

NAM

An activity rate model of induced seismicity within the Groningen Field (Part 2)

Stephen Bourne and Steve Oates

Datum July 2015

Editors Jan van Elk & Dirk Doornhof

General Introduction

A number of alternative seismological models, describing the relationship between compaction and seismicity, have been prepared. In 2013, a strain-partitioning seismological model was presented in the technical addendum to the winningsplan 2013. This model is further described in a scientific peer-reviewed paper titled “A seismological model for earthquakes induced by fluid extraction from a subsurface reservoir”, published in the Journal of Geophysical Research.

As an alternative the new activity rate seismological model was developed. Like the strain-partitioning seismological model, the new activity rate model is based on a statistical analysis of the historical earthquake record data of Groningen, in combination with the measured subsidence above the Groningen field. The model uses a Poisson Point Process model to describe the nucleation rate of earthquakes in response to reservoir compaction and the Epidemic Type Aftershock Sequence model to describe the triggering of additional events.

The new activity rate seismological model achieves more reliable parameter estimates and therefore more precise forecasts than the strain-partitioning model. The model also provide an improved basis to investigate changes in “b-factor” with increasing reservoir depletion and the impact of faults that partially offset the reservoir. The current report describes an extension of the activity rate model.

Both the strain-partitioning seismological model and the alternative activity rate seismological model including the extension of this model have been reviewed by Ian Main, Professor Seismology & Rock Physics at the University of Edinburgh. The innovative elements of the study described in this report will also be published in a peer-reviewed journal. The independent and anonymous experts of the Journal of Geophysical Research will provide further assurance.



NAM

Title	An activity rate model of induced seismicity within the Groningen Field (Part 2)		Date	July 2015
			Initiator	NAM
Autor(s)	Stephen Bourne and Steve Oates	Editors	Jan van Elk Dirk Doornhof	
Organisation	Shell P&T	Organisation	NAM	
Place in the Study and Data Acquisition Plan	<p><u>Study Theme:</u> Seismological Model</p> <p><u>Comment:</u> A number of alternative seismological models have been prepared. In 2013, a strain-partitioning seismological model was presented in the technical addendum to the winningsplan 2013. This model is further described in a scientific peer-reviewed paper titled “A seismological model for earthquakes induced by fluid extraction from a subsurface reservoir”, published in the Journal of Geophysical Research.</p> <p>In the current report an alternative seismological model, an activity rate model, is described. Like the strain-partitioning seismological model, the new activity rate model is based on a statistical analysis of the historical earthquake record data of Groningen, in combination with the measured subsidence.</p>			
Directly linked research	<ul style="list-style-type: none"> (1) Reservoir engineering studies in the pressure depletion for different production scenarios. (2) Seismic monitoring activities; both the extension of the geophone network and the installation on geophones in deep wells. (3) Geomechanical studies. (4) Subsidence and compaction studies. 			
Used data				
Associated organisation	Shell P&T			
Assurance	Review Ian Main, Professor Seismology & Rock Physics at the University of Edinburgh. This report will also be published in a peer-reviewed journal. The independent and anonymous experts of the Journal of Geophysical Research will provide further assurance.			

An activity rate model of seismicity induced
by reservoir compaction and fault reactivation
in the Groningen gas field

S.J.Bourne, S.J. Oates

22 June, 2015

CONFIDENTIAL DRAFT

Abstract

A probabilistic model of seismicity induced by fault reactivation due to reservoir compaction has been developed for short-term forecasting of $M \geq 1.5$ earthquakes induced by gas production from the Groningen gas field. This is based on a simple thin-sheet geomechanical model for the uni-axial tensor strain field due to a continuous distribution of reservoir compaction within the presence of a population of pre-existing faults that partially offset the reservoir. The spatial and temporal distribution of observed seismicity is conformable to this reservoir strain field although only a very small fraction of the induced strains are accommodated by induced earthquakes. The fraction of the reservoir strain accommodated by seismicity increases exponentially with reservoir strain. This is an extension of the earlier activity rate model (Bourne and Oates, 2014) based on the uni-axial scalar strain field represented by reservoir compaction in the presence of a presumed ubiquitous population of mapped and unmapped faults.

As with this earlier activity rate model, aftershocks are included using the Epidemic Type Aftershock Sequence model. Estimation of the joint distribution of all model parameter values that describe the nucleation of independent events and their aftershocks was based on relative likelihoods given the observed events within the historic reservoir strain field. The magnitude of these events are independently distributed according to a constant b -value whose maximum likelihood estimate given the observed magnitudes is $b = 1$. The possibility of a systematic change in b -value with increasing reservoir deformation was also assessed but no evidence was found for any significant changes. Residual differences between the distribution of simulated earthquake catalogues and the observed event origin times, epicenters and magnitudes show no evidence of any statistically significant bias in the performance of this seismological model. If this current relationship between reservoir compaction, reservoir fault geometries and induced seismicity continues then this extended activity rate model offers a reliable basis for probabilistic earthquake forecasting at least in the short term.

1 Introduction

Gas production from the Groningen field has induced earthquakes up to magnitude 3.6. Probabilistic analysis of the seismic hazard associated with gas production plans is a key part of updating future gas production plans (*e.g.* Bourne et al., 2015). The first requirement of such an analysis is a seismological model capable of short-term forecasts for the conditional probability distributions of earthquake numbers, locations, magnitudes and mechanisms given a gas production plan.

Two types of seismological model have been developed for this purpose, both based on forecasts of reservoir compaction strains for a given gas production plan. The choice to use reservoir strain is motivated by the observed spatial-temporal conformance between reservoir strains inferred from geodetic measurements of surface displacements and the measured historic seismicity (Bourne et al., 2014). In contrast, reservoir stress changes due to reservoir pressure depletion, as measured by reservoir pressure gauges, exhibit a distinctly different spatial-temporal pattern. This is attributed to lateral variations in reservoir stiffness associated with reservoir porosity differences.

The strain partitioning model (Bourne et al., 2014) relates the total seismic moment of a catalogue of induced earthquakes to the summed volumetric strain of the reservoir. A compaction dependent strain partitioning factor was introduced into the model to describe the escalating level of seismicity in relation to steady rates of gas production and reservoir compaction. The activity rate model (Bourne and Oates, 2014) is conceptually different in that it describes an inhomogeneous Poisson process for which the number of induced earthquakes is related to the reservoir compaction. Escalation of the seismicity is accommodated by an exponential intensity function for the Poisson process. A second term added to this intensity function describes the contribution from aftershocks according to the Epidemic Type Aftershock Sequence (ETAS) model: the free parameters in the intensity function are estimated by fitting the model to the current Groningen earthquake catalogue. Bourne and Oates (2014) showed that the activity rate model gives a better fit to the Groningen earthquake catalogue to date and that the total seismic moment of the synthetic catalogues generated by it are also consistent with the observations. This is attributed to more robust methods for parameter estimation and a more complete description of the process by including aftershocks.

The reliability of forecasts based on these seismological models depends on the observed historical relationship between induced reservoir strains and induced reservoir seismicity remaining valid over the forecast period. Po-

tential incompleteness of these models will be managed through short-term forecasting, continuous monitoring of reservoir strains and seismicity, and, if necessary, revision of these models. In this report a further development of the Groningen seismicity model is described which includes the effect of strain localization around pre-existing faults that offset the reservoir. This refinement has been developed within the framework of the activity rate model. The key element here is the generalization of the model describing reservoir strains induced by reservoir compaction inferred from geodetic monitoring to include the localisation of shear strains around mapped fault offsets. Consider an idealized model in which a reservoir transected by a vertical weak fault with no throw undergoes uniform compaction. On either side of this fault the uniform reservoir compaction induces no relative displacement of markers in the reservoir, and therefore there is no induced fault slip. If however, there is an initial throw on the fault, markers on either side of the fault will move relative to each other the compaction, although uniform, results in fault slip and this will increase with increasing initial throw. In the following sections this simple observation is developed further and generalized theoretically to show how the maximum seismic moment release rate on a fault is dependent on its throw and how other subsurface topographic features also act to localize reservoir shear strains induced by reservoir compaction and hence also the maximum seismic moment release.

The intensity function for the Poisson process in the original version of the activity rate model (Bourne and Oates, 2014) is expressed in terms of reservoir compaction. Reservoir compaction is the vertical strain-thickness, that is, the product of vertically-averaged vertical strain and reservoir thickness. The activity rate model can be generalized by consideration of the full strain tensor rather than just scalar compaction. In the extended activity rate model the same form is used for the intensity function but instead of compaction, or vertical strain-thickness, the strain-thickness corresponding to the largest eigenvalue of the thin-sheet strain tensor model is used. This is a function of the compaction and the lateral gradients of vertical displacement which, in the case of negligible lateral gradients, reduces to compaction as before. Kostrov's expression for seismic moment release rate due to compaction strains can be generalized to give an equivalent expression in terms of the strain-thickness. Applying the generalized form of the Kostrov expression to the reservoir compaction, fault throw and sub-surface topography data from the Groningen field gives a better correspondence with the spatial distribution of the Groningen earthquake locations than can be achieved with compaction alone.

Using the strain-thickness in the activity rate seismological model is a natural way of including the effect of mapped faults in the PSHA for the

Groningen field. Classical approaches to construction of the source model for PSHA make use of engineering judgment to define source regions around groups of active faults for which averaged levels of seismicity are assumed. In the alternative approach developed here, the map of depth to top reservoir derived from interpretation of the 3D seismic data gives the fault throws and combined with observations of reservoir compaction allows the reservoir strain-thickness to be calculated. The PSHA workflow is then developed based on the strain-thickness to address the question of the extent to which induced earthquakes occur preferentially on mapped faults without the need to make choices of how zones of different seismic activity should be defined.

2 Models of compaction-induced fault strain

2.1 A simple discrete-fault strain model

Considering the simple case of uniform uni-axial compaction within a reservoir of uniform thickness and infinite lateral extent offset by a vertical fault of uniform offset as shown in Figure 1. The maximum total seismic moment per unit strike length of this fault is then simply

$$\mathcal{M}_s = \mu \int (u_1 - u_2) dz \quad (1)$$

where μ is the elastic shear modulus of the medium. This integral is simply the area between the two displacement profiles located on either side of the

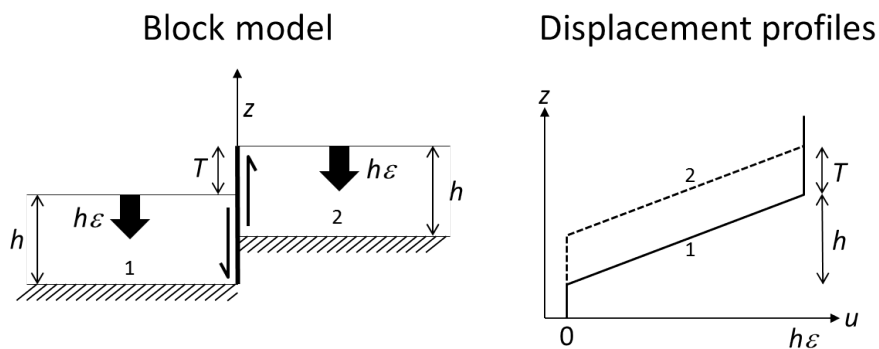


Figure 1: Simple block model of uniform uni-axial compaction within a reservoir offset by a vertical fault. Differences between profiles of the vertical displacement due to uni-axial reservoir compaction on either side of the fault represent the maximum slip potential for an unlocked vertical fault.

fault. Consequently,

$$\mathcal{M}_s = \mu T h \epsilon = \mu T c \quad (2)$$

where T is the fault offset, h is the reservoir thickness and ϵ is the uniform uni-axial reservoir compaction strain. So, we recognize the maximum seismic moment per unit strike length scales with the product of reservoir compaction, $c = h\epsilon$ and fault offset.

The slip patch on this fault may not be entirely seismogenic. If, for instance, portions of the fault juxtapose to the geological top seal undergo stable sliding then the seismic moment will be restricted to the slip patch within and below the reservoir. Likewise, the same may also be true for the formation directly below the reservoir, in which case seismogenic slip will be restricted to the slip patch within the reservoir. The geometry of these two restricted cases (Figure 2) means the seismic moment per unit strike length

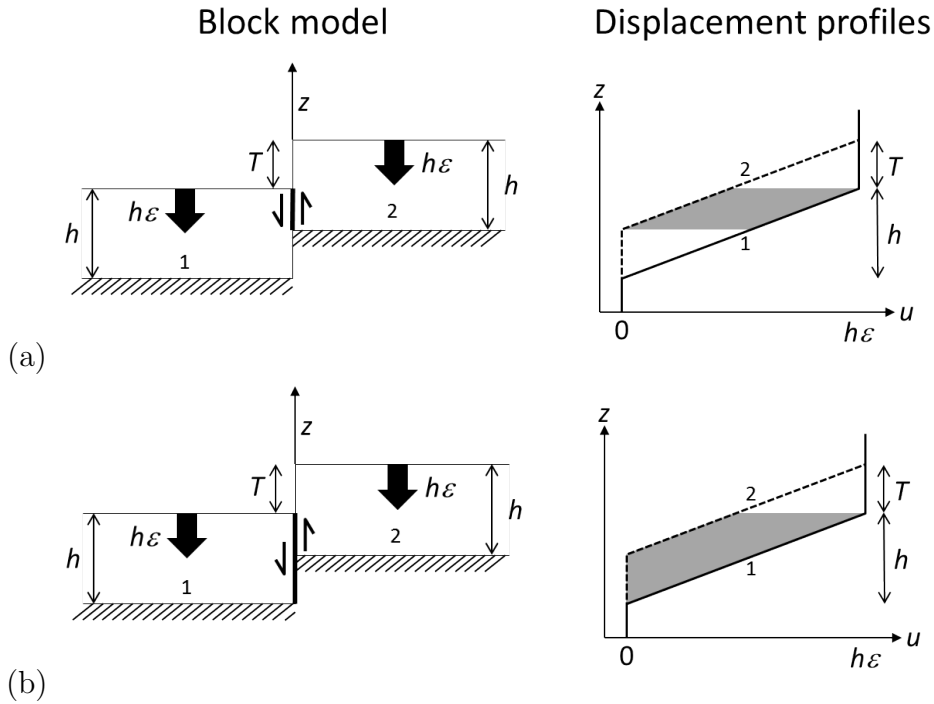


Figure 2: Restricted versions of the simple block model shown in Figure 1. (a) Only fault slip within the reservoir is seismogenic. (b) Only fault slip within or below the reservoir is seismogenic. In both cases, the seismic moment per unit fault length equates to the shaded area between the displacement profiles on either side of the fault.

for seismogenic slip within the reservoir is

$$\mathcal{M}_{s,1} = \begin{cases} \mu T c (1 - \frac{T}{h}), & \text{if } T \leq h \\ 0, & \text{if } T > h, \end{cases} \quad (3)$$

and for seismogenic slip within and below the reservoir

$$\mathcal{M}_{s,2} = \begin{cases} \mu T c (1 - \frac{1}{2} \frac{T}{h}), & \text{if } T \leq h \\ \frac{1}{2} \mu T c, & \text{if } T > h. \end{cases} \quad (4)$$

2.2 A thin-sheet continuum strain model

Let us now consider the general conditions of uni-axial reservoir compaction where the displacement vector is $\mathbf{u} = (0, 0, u_z)$. For the thin-sheet reservoir geometry shown in Figure 3 with its base at elevation z_o and its top at elevation $z_o + h$, the vertical displacement profile depends on elevation as

$$u_z = \begin{cases} h \epsilon_{zz}, & \text{if } z \geq z_o + h \\ (z - z_o) \epsilon_{zz}, & \text{if } z_o \leq z < z_o + h \\ 0, & \text{if } z < z_o \end{cases} \quad (5)$$

where the vertical strain $\epsilon_{zz} = \frac{\partial u_z}{\partial z}$. In general, the reservoir strain, ϵ_{zz} , the base reservoir elevation, z_o and the reservoir thickness, h , will all be continuous functions of position.

The strain tensor, defined as $\epsilon_{ij} = \frac{1}{2} \left(\frac{\partial u_i}{\partial x_j} + \frac{\partial u_j}{\partial x_i} \right)$, which for uni-axial compaction reduces to

$$\epsilon_{ij} = \frac{1}{2} \begin{pmatrix} 0 & 0 & \frac{\partial u_z}{\partial x} \\ 0 & 0 & \frac{\partial u_z}{\partial y} \\ \frac{\partial u_z}{\partial x} & \frac{\partial u_z}{\partial y} & 2 \frac{\partial u_z}{\partial z} \end{pmatrix}. \quad (6)$$

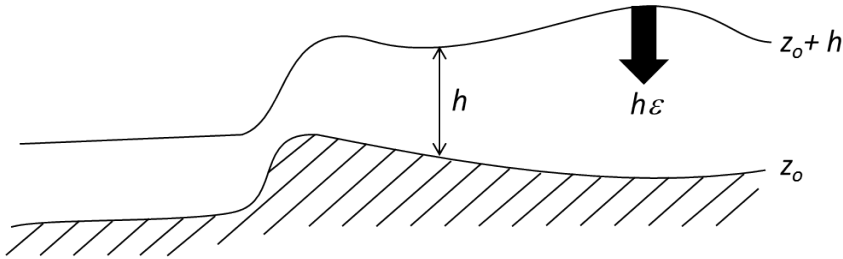


Figure 3: General model of uni-axial compaction within a thin-sheet reservoir geometry.

The partial derivatives of displacement that contribute to the strain tensor inside the reservoir follow as

$$\begin{aligned}\frac{\partial u_z}{\partial x} &= -\epsilon_{zz} \frac{\partial z_o}{\partial x} + (z - z_o) \frac{\partial \epsilon_{zz}}{\partial x}, \\ \frac{\partial u_z}{\partial y} &= -\epsilon_{zz} \frac{\partial z_o}{\partial y} + (z - z_o) \frac{\partial \epsilon_{zz}}{\partial y}, \\ \frac{\partial u_z}{\partial z} &= \epsilon_{zz}.\end{aligned}\tag{7}$$

The vertically averaged strain inside the reservoir is

$$\bar{\epsilon}_{ij} = \frac{1}{h} \int_{z_o}^{z_o+h} \epsilon_{ij} dz.\tag{8}$$

Combing equations (6), (7) and (8) leads to the following expressions for the non-zero elements of the average strain tensor:

$$\begin{aligned}\bar{\epsilon}_{xz} &= -\frac{\epsilon_{zz}}{2} \left(\frac{\partial z_o}{\partial x} \right) + \frac{h}{4} \left(\frac{\partial \epsilon_{zz}}{\partial x} \right), \\ \bar{\epsilon}_{yz} &= -\frac{\epsilon_{zz}}{2} \left(\frac{\partial z_o}{\partial y} \right) + \frac{h}{4} \left(\frac{\partial \epsilon_{zz}}{\partial y} \right), \\ \bar{\epsilon}_{zz} &= \epsilon_{zz}.\end{aligned}\tag{9}$$

Alternatively, these same expressions may be rewritten as derivatives of the observable quantities of base reservoir topography, z_o , reservoir thickness, c , and reservoir compaction, c , where $c = -h\epsilon_{zz}$ as follows.

$$\begin{aligned}\bar{\epsilon}_{xz} &= -\frac{\epsilon_{zz}}{2} \left(\frac{\partial z_o}{\partial x} \right) - \frac{\epsilon_{zz}}{4} \left(\frac{\partial h}{\partial x} \right) - \frac{1}{4} \left(\frac{\partial c}{\partial x} \right), \\ \bar{\epsilon}_{yz} &= -\frac{\epsilon_{zz}}{2} \left(\frac{\partial z_o}{\partial y} \right) - \frac{\epsilon_{zz}}{4} \left(\frac{\partial h}{\partial y} \right) - \frac{1}{4} \left(\frac{\partial c}{\partial y} \right), \\ \bar{\epsilon}_{zz} &= \epsilon_{zz},\end{aligned}\tag{10}$$

This yields a vertically-averaged strain tensor

$$\bar{\epsilon}_{ij} = \begin{pmatrix} 0 & 0 & \bar{\epsilon}_{xz} \\ 0 & 0 & \bar{\epsilon}_{yz} \\ \bar{\epsilon}_{xz} & \bar{\epsilon}_{yz} & \bar{\epsilon}_{zz} \end{pmatrix}.\tag{11}$$

The eigenvalues of this tensor are

$$\begin{aligned}\lambda_{1,3} &= \frac{\bar{\epsilon}_{zz}}{2} \left(1 \pm \sqrt{1 + \Gamma^2} \right), \\ \lambda_2 &= 0,\end{aligned}\tag{12}$$

where

$$\Gamma^2 = 4 \frac{\bar{\epsilon}_{xz}^2 + \bar{\epsilon}_{yz}^2}{\bar{\epsilon}_{zz}^2}. \quad (13)$$

The corresponding orthogonal eigenvectors are:

$$\begin{aligned} \hat{n}_{1,3} &= [\bar{\epsilon}_{xz}, \bar{\epsilon}_{yz}, \lambda_{1,3}], \\ \hat{n}_2 &= [\bar{\epsilon}_{yz}, -\bar{\epsilon}_{xz}, 0]. \end{aligned} \quad (14)$$

In this reference frame, the vertically-averaged principal strain tensor is then simply

$$\bar{\epsilon}_{ij} = \begin{pmatrix} \lambda_1 & 0 & 0 \\ 0 & 0 & 0 \\ 0 & 0 & \lambda_3 \end{pmatrix}. \quad (15)$$

For the trace-free deviatoric strain tensor, *i.e.* $\epsilon_{ij} - \frac{1}{3}\delta_{ij}\epsilon_{kk}$ where δ_{ij} is the Kronecker delta, the eigenvalues are then:

$$\begin{aligned} \lambda'_{1,3} &= \frac{\bar{\epsilon}_{zz}}{2} \left(\frac{1}{3} \pm \sqrt{1 + \Gamma^2} \right), \\ \lambda'_2 &= -\frac{\bar{\epsilon}_{zz}}{3}. \end{aligned} \quad (16)$$

The corresponding orthogonal eigenvectors are:

$$\begin{aligned} \hat{n}_{1,3} &= [\bar{\epsilon}_{xz}, \bar{\epsilon}_{yz}, \frac{\bar{\epsilon}_{zz}}{2} (1 \pm \sqrt{1 + \Gamma^2})], \\ \hat{n}_2 &= [\bar{\epsilon}_{yz}, -\bar{\epsilon}_{xz}, 0], \end{aligned} \quad (17)$$

In this reference frame, the vertically-averaged principal deviatoric strain tensor is then simply

$$\bar{\epsilon}'_{ij} = \begin{pmatrix} \lambda'_1 & 0 & 0 \\ 0 & \lambda'_2 & 0 \\ 0 & 0 & \lambda'_3 \end{pmatrix}. \quad (18)$$

Following Kostrov (1974), the incremental average irrotational seismic strain, $\bar{\epsilon}_s$, due to a population of earthquakes that occurred within a given volume and a given time interval is proportional to the sum of their seismic moment tensors,

$$\bar{\epsilon}_{s,ij}(t) = \frac{1}{2\mu V} \sum_{k=1}^{N(t)} M_o^k m_{ij}^k, \quad (19)$$

where $\bar{\epsilon}_{s,ij}$ is the ij^{th} component of the average seismic strain tensor, N is the number of events that occurred within the given volume, V , and the

time interval, t , μ is the shear modulus, M_o^k and m_{ij}^k are the scalar seismic moment and the unit symmetric moment tensor of the k^{th} event respectively.

Equating the vertically-averaged strain tensor with the maximum total seismic moment per unit area leads to

$$\frac{1}{A} \sum_{k=1}^{N(t)} M_o^k m_{ij}^k = 2\mu h \bar{\epsilon}_{s,ij}(t), \quad (20)$$

where A is the horizontal area occupied by the given volume, V , and $\bar{\epsilon}$ becomes the average strain within this volume. Combining this with the expression for principal strain tensor given by (18) yields

$$\frac{1}{A} \sum_{k=1}^{N(t)} M_o^k m_{ij}^k = \mu h \bar{\epsilon}_{zz} \left(1 + \sqrt{1 + \Gamma^2}\right) \begin{pmatrix} 1 & 0 & 0 \\ 0 & 0 & 0 \\ 0 & 0 & \frac{\lambda_3}{\lambda_1} \end{pmatrix}, \quad (21)$$

Alternatively, if the seismicity only relates to the principal deviatoric strain tensor, *i.e.* earthquakes play no part in accommodating the isotropic strain, then (20) combines with (16) such that

$$\frac{1}{A} \sum_{k=1}^{N(t)} M_o^k m_{ij}^k = \mu h \bar{\epsilon}_{zz} \left(\frac{1}{3} + \sqrt{1 + \Gamma^2}\right) \begin{pmatrix} 1 & 0 & 0 \\ 0 & \frac{\lambda'_2}{\lambda'_1} & 0 \\ 0 & 0 & \frac{\lambda'_3}{\lambda'_1} \end{pmatrix}, \quad (22)$$

Now let us consider the special case where lateral gradients in reservoir thickness and lateral gradients in reservoir compaction are small relative to the lateral gradients in the elevation of the base reservoir equation (10) may be approximated as

$$\begin{aligned} \bar{\epsilon}_{xz} &\approx -\frac{\epsilon_{zz}}{2} \left(\frac{\partial z_o}{\partial x}\right), \\ \bar{\epsilon}_{yz} &\approx -\frac{\epsilon_{zz}}{2} \left(\frac{\partial z_o}{\partial y}\right), \\ \bar{\epsilon}_{zz} &= \epsilon_{zz}. \end{aligned} \quad (23)$$

In this case, the maximum seismic moments per unit area required to accommodate the deviatoric strains are

$$\frac{1}{A} \sum_{k=1}^{N(t)} M_o^k m_{ij}^k = -\mu c(t) \left(\frac{1}{3} + \sqrt{1 + |\nabla(z_o)|^2}\right) \begin{pmatrix} 1 & 0 & 0 \\ 0 & \frac{\lambda'_2}{\lambda'_1} & 0 \\ 0 & 0 & \frac{\lambda'_3}{\lambda'_1} \end{pmatrix}, \quad (24)$$

where

$$|\nabla(z_o)|^2 = \left(\frac{\partial z_o}{\partial x}\right)^2 + \left(\frac{\partial z_o}{\partial y}\right)^2. \quad (25)$$

Let us now compare this with the expression previously obtained from the simple model for the maximum seismic moment per unit strike length given by (2). Consider a single vertical fault oriented parallel to the y -axis such that $\frac{\partial z_o}{\partial y} = 0$. From (24), the maximum seismic moment per unit strike length is, in the limit that $\Delta x \ll T$ is

$$\begin{aligned} \mathcal{M}_s &\approx \Delta x \mu c(t) \left(\frac{1}{3} + \sqrt{1 + \left(\frac{\partial z_o}{\partial x}\right)^2} \right), \\ &\approx \mu c \left(\frac{\Delta x}{3} + \sqrt{\Delta x^2 + T^2} \right), \\ &\approx \mu c T. \end{aligned} \quad (26)$$

This is exactly the result previously obtained from the simple model.

Furthermore, returning to (24), if lateral gradients in the elevation of the base reservoir are also negligible this then reduces to

$$\sum_{k=1}^{N(t)} M_o^k m_{ij}^k = \frac{4}{3} \mu \Delta V(t) \begin{pmatrix} 1 & 0 & 0 \\ 0 & -\frac{1}{2} & 0 \\ 0 & 0 & -\frac{1}{2} \end{pmatrix}, \quad (27)$$

such that $\Delta V = A\bar{c}$, and \bar{c} is the average reservoir compaction within the given volume V . This is recognizable as the relationship previously described by Bourne et al. (2014) for the maximum seismic moment induced by a bulk reservoir volume change.

To facilitate a direct connection with the previous activity rate model based on an exponential trend with reservoir compaction (Bourne and Oates, 2014), we recognize that reservoir compaction is the vertical strain thickness, *i.e.* $c = \bar{\epsilon}_{zz} h$ where $\bar{\epsilon}_{zz}$ is the vertically-averaged vertical strain and h is the reservoir thickness. Similarly, the strain-thickness corresponding to the largest eigenvalue of the thin-sheet strain tensor model is

$$c_t = c(t) \left(\frac{1}{3} + \sqrt{1 + |\nabla(z_o)|^2} \right) \quad (28)$$

Consequently, the Poisson intensity function that describes the probability density of earthquake nucleation is unchanged, except that strain thickness, c_t replaces compaction, c , such that

$$\lambda(\mathbf{x}, t) = \beta_0 \dot{c}_t (1 + \beta_1 c_t) e^{\beta_1 c_t}, \quad (29)$$

Finally, we introduce a weighting scheme to allow for systematic testing of the relative importance of strain localized on mapped faults due to their offsets versus the distributed strain of the compaction field that may act on preexisting unmapped faults. This is also necessary because topographic gradients and fault offset interpretations are subject to some unknown degree of smoothing due to resolution limited in the seismic image. The weighting scheme is applied as

$$c_t = c(t) \left(\frac{1}{3}w_c + \sqrt{w_c + w_t|\nabla(z_o)|^2} \right), \quad (30)$$

where $w_c = 1 - w_t$. If $w_c = 1$, the weighting scheme reduces the strain thickness to the expression due to reservoir compaction alone, as given by (27). Alternatively, if $w_t = 1$, the weighting scheme reduces the strain thickness to the result due to fault offsets alone, as given by (26).

3 Application to the Groningen field

3.1 Seismicity and subsidence

Surface subsidence observed by optical levelling networks between 1964 and 2013 indicate the region of largest surface subsidence are closely associated with the region of largest observed seismicity (*e.g.* Figure 4). The large fraction of earthquake epicenters preferentially located with the small region of the field subjected to the largest surface subsidence cannot simply be coincidence. Clearly, within the Groningen field, seismogenic fault-slip plays some role in accommodating reservoir strains induced by reservoir pressure depletion.

Due to the limited number of levelling benchmarks located within the

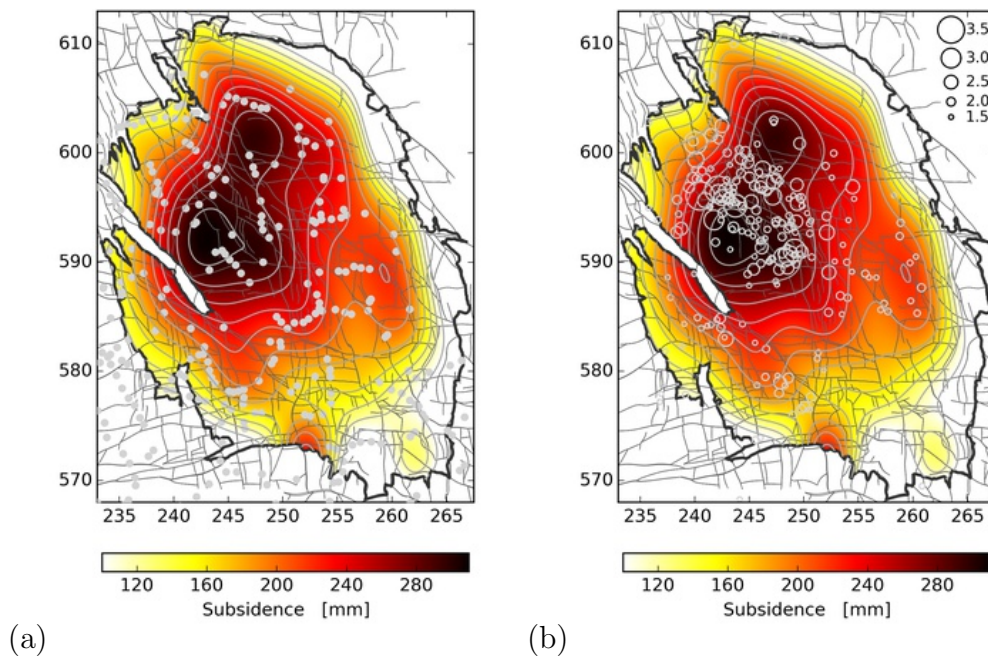


Figure 4: (a) Surface subsidence as measured by geodetic surveys acquired in September 1972 and December 2011. Grey circles denote the survey benchmarks. These data are interpolated between the survey benchmarks using a smooth bi-cubic spline inside the field boundary. (b) The same surface subsidence in relation to the observed earthquake epicentres from 1 April 1995 to 18 January 2015. The area of each circle denotes the magnitude of the earthquake according to the legend shown. Light grey lines denote subsidence contours and dark grey lines denote fault traces mapped at the Top Rotliegendes horizon.

region of greatest surface subsidence there is some remaining uncertainty about the exact location of maximum subsidence. Equally, due to the relatively small total number of observed epicenters the exact location of greatest seismicity is also uncertain. Based on the levelling data, the center of maximum subsidence appears to be located 2–5 km to the south of the region of greatest seismicity (*e.g.* Figure 4b). This evidence for a possible offset between the centers of subsidence and seismicity is significant because it implies that a seismological model based only on reservoir compaction may be incomplete as some additional mechanism, perhaps related to the observed fault geometries, is required to explain this apparent eccentricity.

InSAR, however, provides alternative independent measurements of surface displacements with significantly greater spatial and temporal sampling, may yield a slightly different result where the center of subsidence and seismicity are essentially co-located (*e.g.* Figure 5). Further work is ongo-

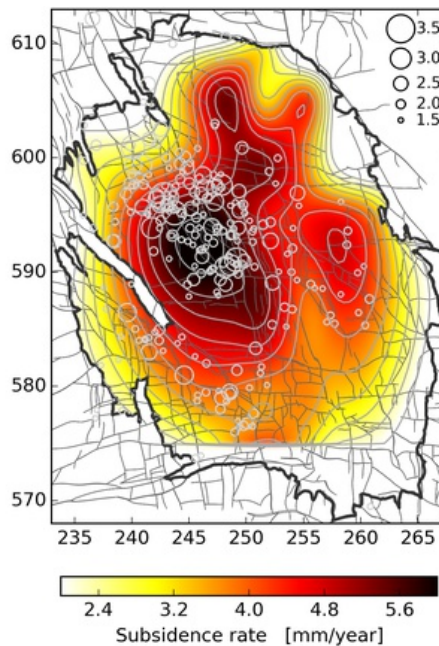


Figure 5: Contoured values of average InSAR subsidence rate compared to earthquakes. These subsidence rates are based on combining the average rate of Envisat ascending and descending line-of-sight displacements. Ascending track data are from 25-Jun-2006 to 8-Aug-2010. Descending track data are from 21-Dec-2003 to 5-Sep-2010. All $M_L \geq 1.5$ earthquakes are shown from 1-Apr-1995 to 18-Jan-2015. Subsidence rates below northing coordinate 575 km are not shown due to the influence of another nearby field.

ing to improve the use of InSAR measurements for constraining reservoir compaction models in order to further assess the validity of the existing compaction-based seismological models (Bourne et al., 2014; Bourne and Oates, 2014).

3.2 Seismicity and reservoir compaction

Surface subsidence observed by optical levelling networks are for the most-part consistent with a locally constant rate of reservoir compaction with reservoir pressure depletion (Bierman et al., 2015). Inversion of these levelling data yields a spatial distribution of time-invariant compressibility thickness given information about the vertically-averaged reservoir pressure depletion obtained from matching the dynamic reservoir model for fluid transport to the observed history of gas production and reservoir pressure depletion. A reservoir compaction model then follows simply as the product of vertically-average reservoir pressure depletion time series and the compressibility thick-

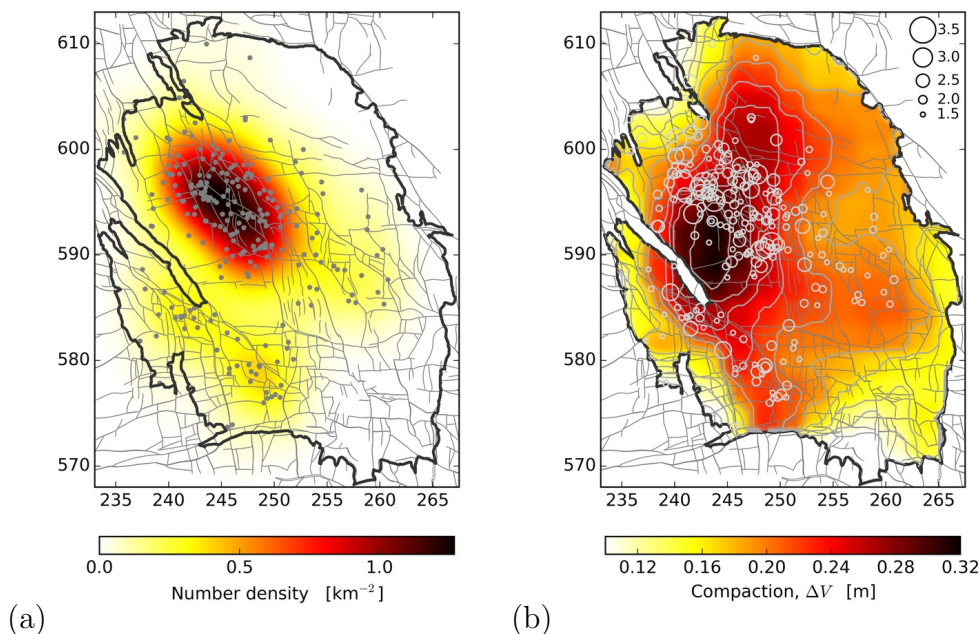


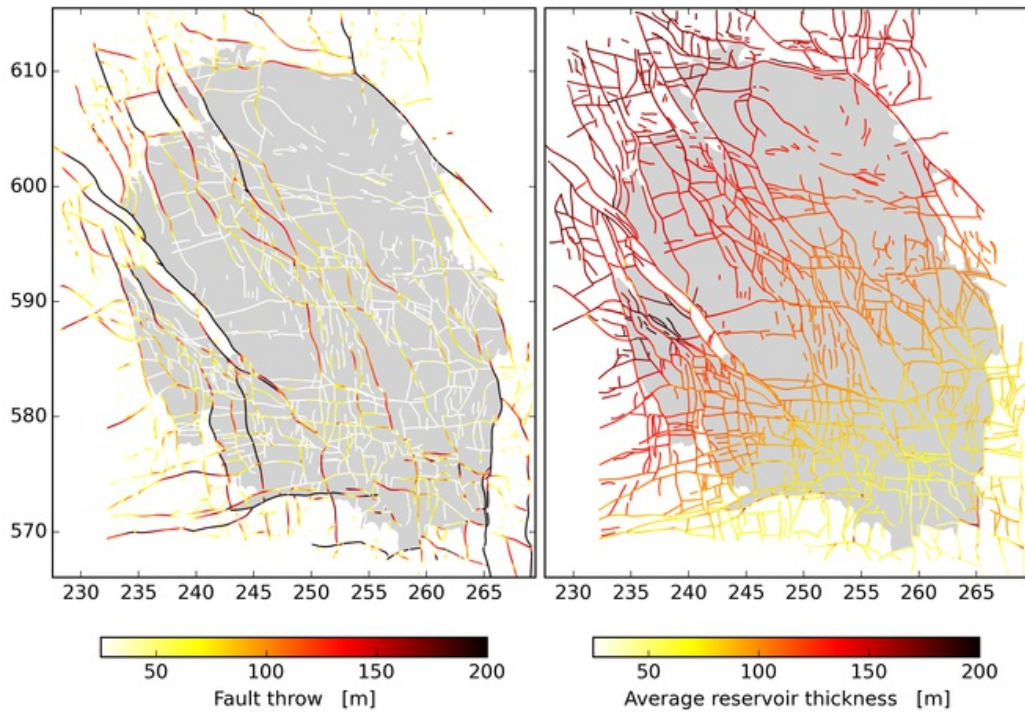
Figure 6: (a) Observed epicenters of $M_L \geq 1.5$ events from 1 April 1995 to 18 January 2015. The underlying event number density function was estimated using the Gaussian kernel density method. (b) The same epicenters shown in relation to reservoir compaction estimated by inversion of the geodetic levelling data (Bierman et al., 2015). The area of the circles denotes event magnitude as indicated in the legend.

ness map.

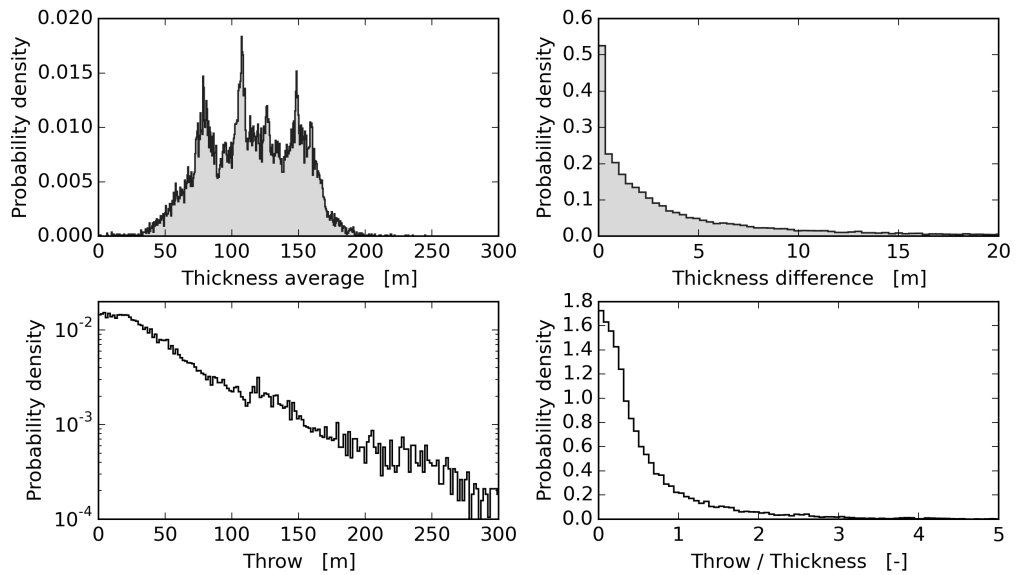
The relationship between reservoir compaction and surface displacements is governed by the geomechanical response of the subsurface to reservoir compaction. A point source of reservoir volume change causes a surface displacements with a dominant spatial wavelength commensurate with the depth of the reservoir below the surface. Consequently, the subsurface acts like a low-pass filter so any image of reservoir compaction obtained from surface displacement measurements will have a lateral resolution length-scale comparable to the reservoir depth (3 km). Consequently, the resulting compaction model is spatially smoothed using cross-validation to ensure optimum predictive power within the limitations of the levelling data (Bierman et al., 2015).

Figure 6 compares this compaction model with a measure of earthquake number density. Again, we observed evidence of a small offset between the center of reservoir compaction and the center of seismicity. Results from inversion of the InSAR data to further constrain the reservoir compaction model are expected to reduced uncertainty in this evidence due to the limited spatial sampling provided by the levelling data. Nonetheless, it already seems clear that the contours of earthquake number density define a region that is elongated along the region fault strike (northwest-southeast), whereas both the levelling and InSAR data suggest the region of greatest reservoir compaction is elongated perpendicular to the regional fault strike (northeast-southwest).

Furthermore, there is emerging evidence for two distinct regions of seismicity, the main central region (located around 245,595) and a smaller, less active region (located around 245, 580) separated by a northwest-southeast oriented zone with limited or no seismicity. This zone contains many fewer mapped faults than the adjacent seismically active regions. These two observations seem sufficient motivation to consider further how these fault geometries might play a role in governing the induced strain field that drives the induced seismicity.



(a)



(b)

Figure 7: (a) Maps of interpreted throw measured at the top Rotliegendes horizon and reservoir thickness measured at each fault location. (b) The observed frequency distribution of the average reservoir thickness on either side of faults, the difference in reservoir thickness across faults, fault throws, and the ratio of fault throws to average reservoir thickness.

3.3 Distribution of fault throws

The simple block model and the continuum thin-sheet model of strains induced by reservoir compaction in the presence of preexisting vertical faults indicates the simple shear strains due to the presence of these faults (ϵ_{xz} , ϵ_{yz}) are equal to the product of reservoir compaction and fault throw. Both of these properties are reasonably well-known to use from direct observations; reservoir compaction from inversion of the geodetic data and fault throws from interpretation of the reflection seismic image.

The largest fault throws are at least 200 m and these are mostly located along the lateral boundaries of the gas reservoir (Figure 7). As is typical for geological fault populations, the frequency distribution of fault throws follows an power-law with many more faults with smaller throws than larger throws. This distribution also indicates that faults below 25 m throws are below the detection threshold of the seismic image. Although these smaller faults are not detected, the power-law distribution suggests they are likely

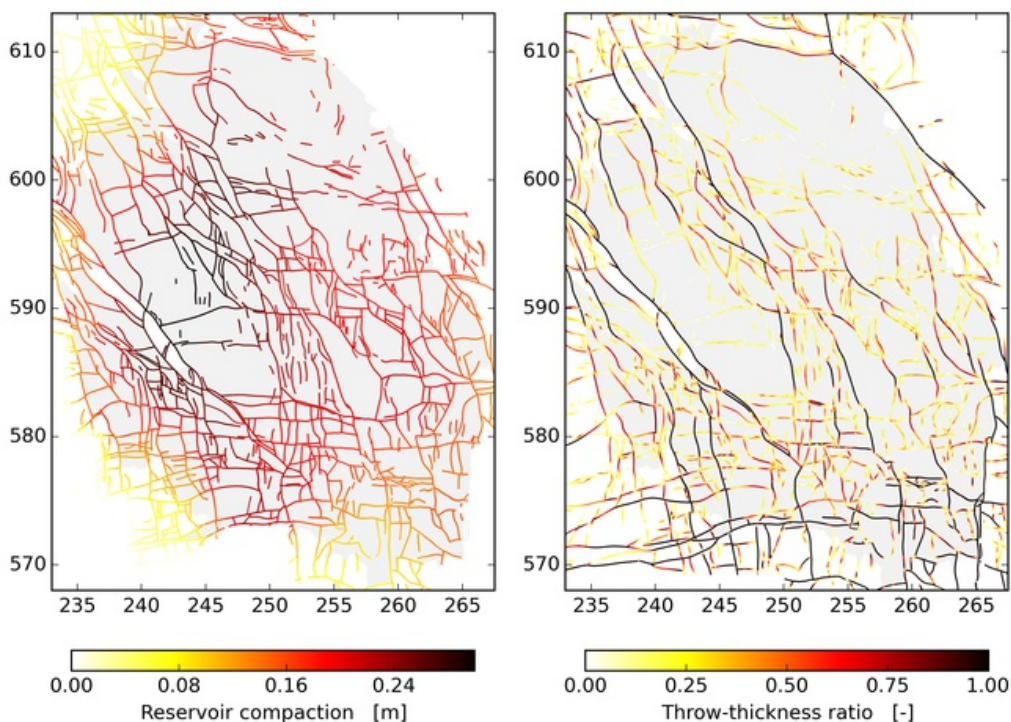


Figure 8: Reservoir compaction (left) and fault throw to reservoir thickness ratios (right) at the location of each fault mapped at the top of the Rotliegendes horizon.

to be present in even greater numbers than the mapped faults.

The presence of any discontinuous changes in reservoir thickness across faults would imply discontinuous changes in reservoir compaction across these faults even under conditions of uniform pressure depletion and reservoir compressibility. Any such compaction discontinuities would also be a mechanism for inducing fault slip outside the reservoir. The observed distribution of thickness differences is much smaller than the detection threshold of about 25 m, and so on this basis is considered to be insignificant. This suggests reservoir compaction is likely to be continuous across faults.

Figure 8 shows maps of reservoir compaction at the location of mapped faults and the fault throw to reservoir thickness ratio to indicate which faults partially or completely offset the reservoir. As reservoir thickness is smallest in the south and southeast parts of the reservoir (Figure 7), it follows that most faults that completely offset the reservoir are located in this region. Elsewhere, only a few of the largest faults completely offset the reservoir.

3.4 Distribution of topographic gradients

The thin-sheet continuum strain model is formulated in terms of topographic gradients of the top reservoir horizon. These gradients were estimated using a finite-difference operator on the top Rotliegendes horizon interpreted from the seismic image on a 50 by 50 m grid (Figure 9). Results indicate the largest topographic gradients exactly conform to the mapped fault locations and yield gradients that are equivalent to the mapped fault throws converted to an equivalent topographic gradient on a 50 by 50 m grid.

Small differences are apparent between these two maps (Figures 9c and 9d) but these typically related to the smallest fault throws that are close to the detection threshold of the seismic image. In these places the differences may be attributed to interpretation choices in the presence of noise. Nonetheless, as the thin-sheet strain model is most sensitive to larger fault throws, these differences for the smallest faults throws are not expected to be influential in the application of this model.

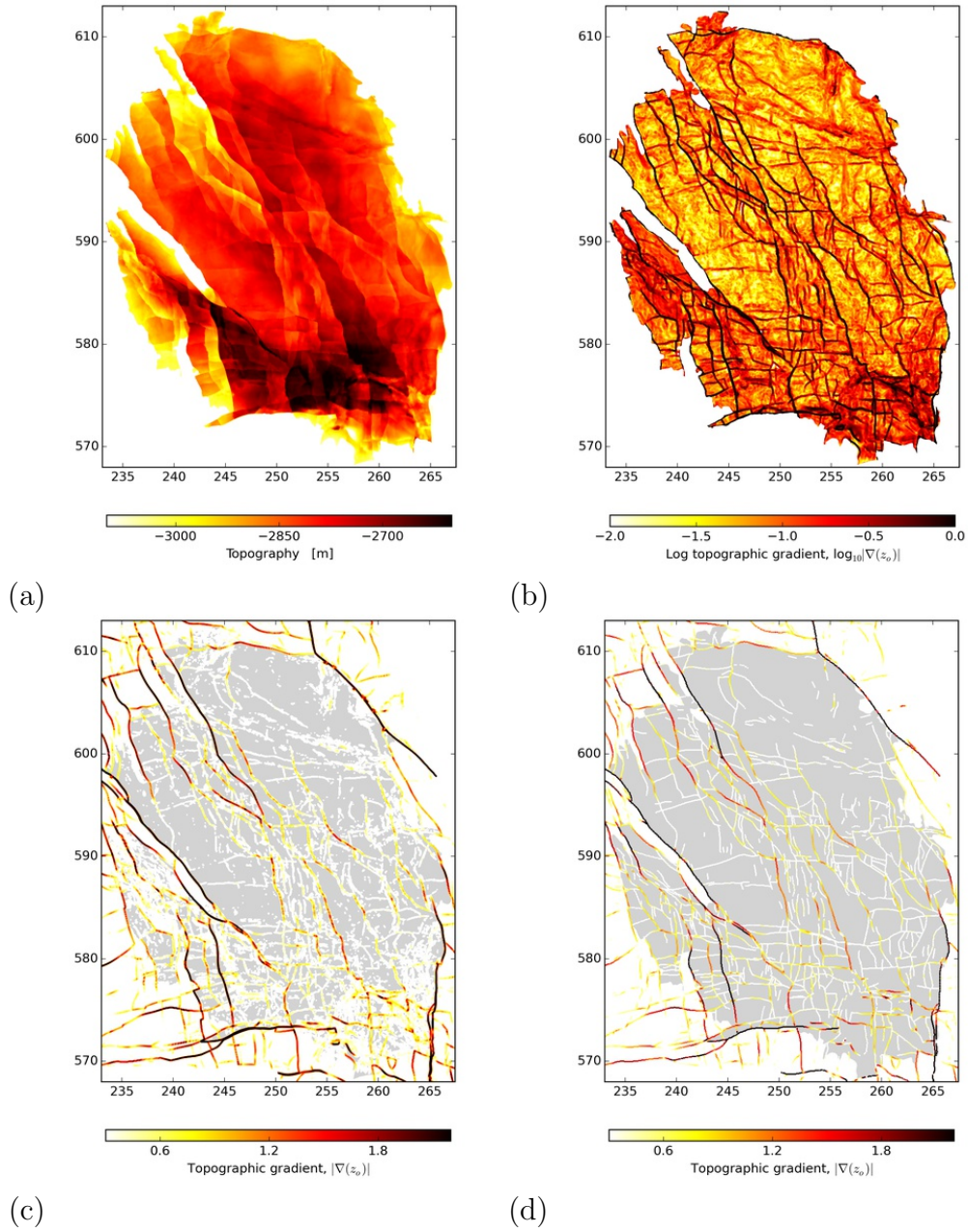


Figure 9: (a) Topography of the top reservoir horizon mapped from the reflection seismic image. (b, c) Topographic gradients of the top reservoir horizon computed as finite-differences on a 50 by 50 m grid and shown on a logarithmic and linear color scales respectively. (d) Topographic gradients computed from the measured throws of mapped faults on the same 50 by 50 m grid.

3.5 Application of the simple discrete-fault strain model

The simple block model of maximum seismic moment per unit strike length (2) predicts that mapped faults with the largest product of reservoir compaction and fault throw should be the most seismogenic. Figure 10a shows the application of this model to the Groningen reservoir where many of the faults with large values of maximum seismic moment density are located within the region of larger earthquake number density. There are however notable exceptions, for instance the large boundary fault located directly to the southwest of this region is predicted to have one of the largest maximum seismic moment density of any mapped fault but there is a clear absence of observed seismicity within the vicinity of this fault. This may be because the reservoir compaction at this location is over-estimated due to smoothing or bias within the compaction model obtained from inversion of the levelling data. Alternatively, the fault may be experiencing predominately aseismic slip, perhaps because its throw completely offsets the reservoir.

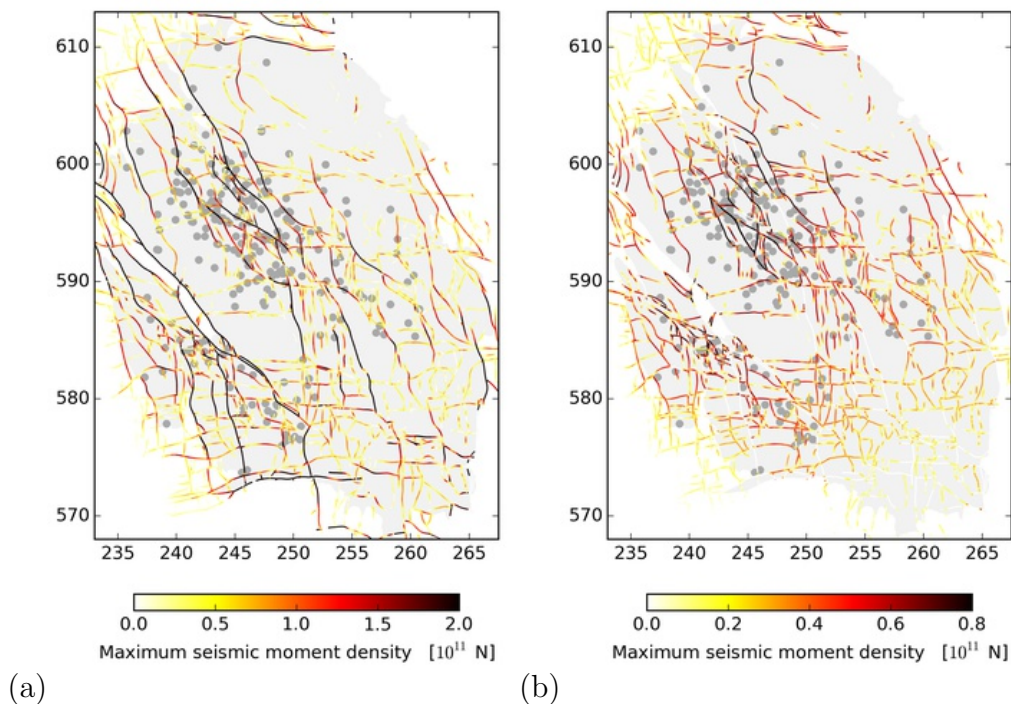


Figure 10: Maximum seismic moment density computed according to the discrete-fault block-model for two scenarios: (a) all fault slip is seismogenic, (b) only fault slip within the reservoir is seismogenic. Grey circle denote the epicenter of all $M_L \geq 1.5$ events located between 1 April 1995 and 18 January 2015.

Considering the alternative simple block model where only fault slip within the reservoir is seismogenic (3) the resulting maximum seismic moment density map appears to show improved conformance with the observed epicenters and notably the maximum seismic moment associated with this particular boundary fault is reduced to zero. These results from the simple block model are promising so let us now proceed to the application of the more-general thin-sheet strain model.

3.6 Application of the thin-sheet strain model

Before proceeding to calibrate the activity rate parameters of the thin-sheet strain model (β_0, β_1) to the observed space-time distribution of earthquake epicenters we should first consider the limitations imposed by the finite sample size ($N = 230$) and standard epicenter location errors (500 m). The small number of observed epicenters means the underlying probability distribution is sparsely sampled and so may only be reliably estimated subject to some degree of spatial smoothing. The true probability density distribution may be highly localized on preexisting faults but our current information lacks the spatial resolution to demonstrate this. Instead we seek the smoothest distribution consistent with the observed epicenters to avoid the potential for bias by including additional information not justified by observations. Likewise, as the standard epicenter location error is similar to the typical spacing of mapped faults there is an additional limitation to the spatial resolution we may achieve in the seismological model.

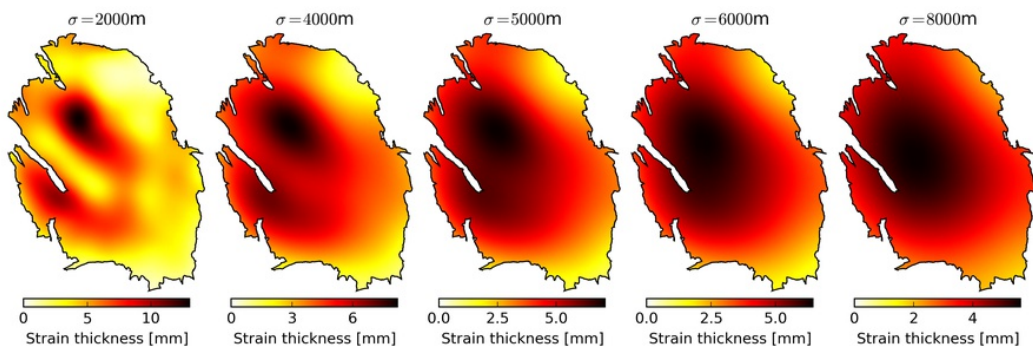


Figure 11: Reservoir strain thickness computed according to the thin sheet continuum model for $w_t = 1$, and then smoothed using Gaussian filter kernels with standard deviations (σ) increasing from 250 m to 3000 m. All faults with throws exceeding the reservoir thickness were excluded from the model.

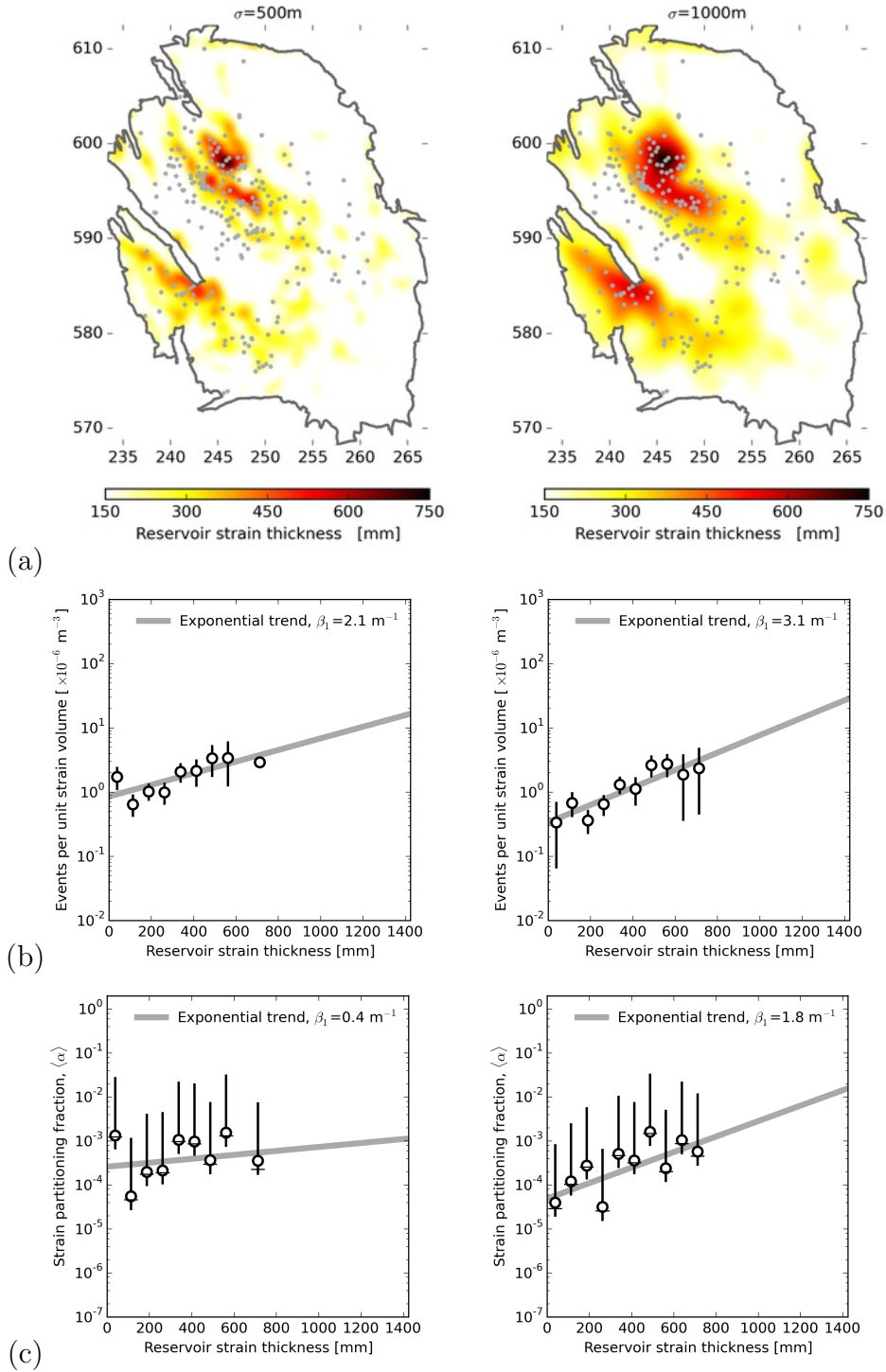


Figure 12: (a) Reservoir strain thickness ($\sigma = 500, 1000 \text{ m}$) and epicenters (1995-2015, $M_w \geq 1.5$). (b, c) Activity rate and strain partitioning versus reservoir strain thickness. Fault throws exceeding reservoir thickness were excluded.

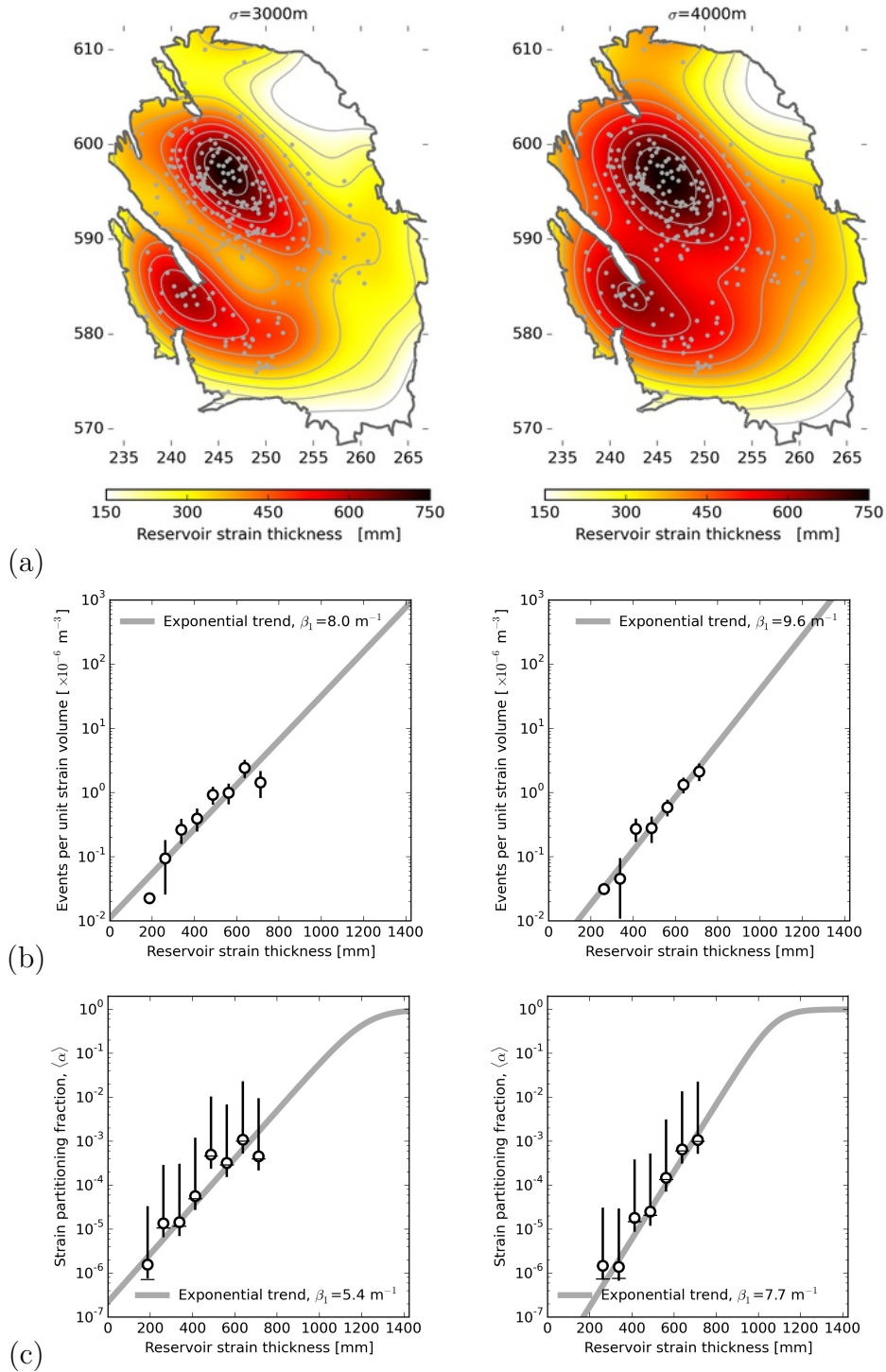


Figure 13: As Figure 12, except for $\sigma = 3000 \text{ m}$ and 4000 m .

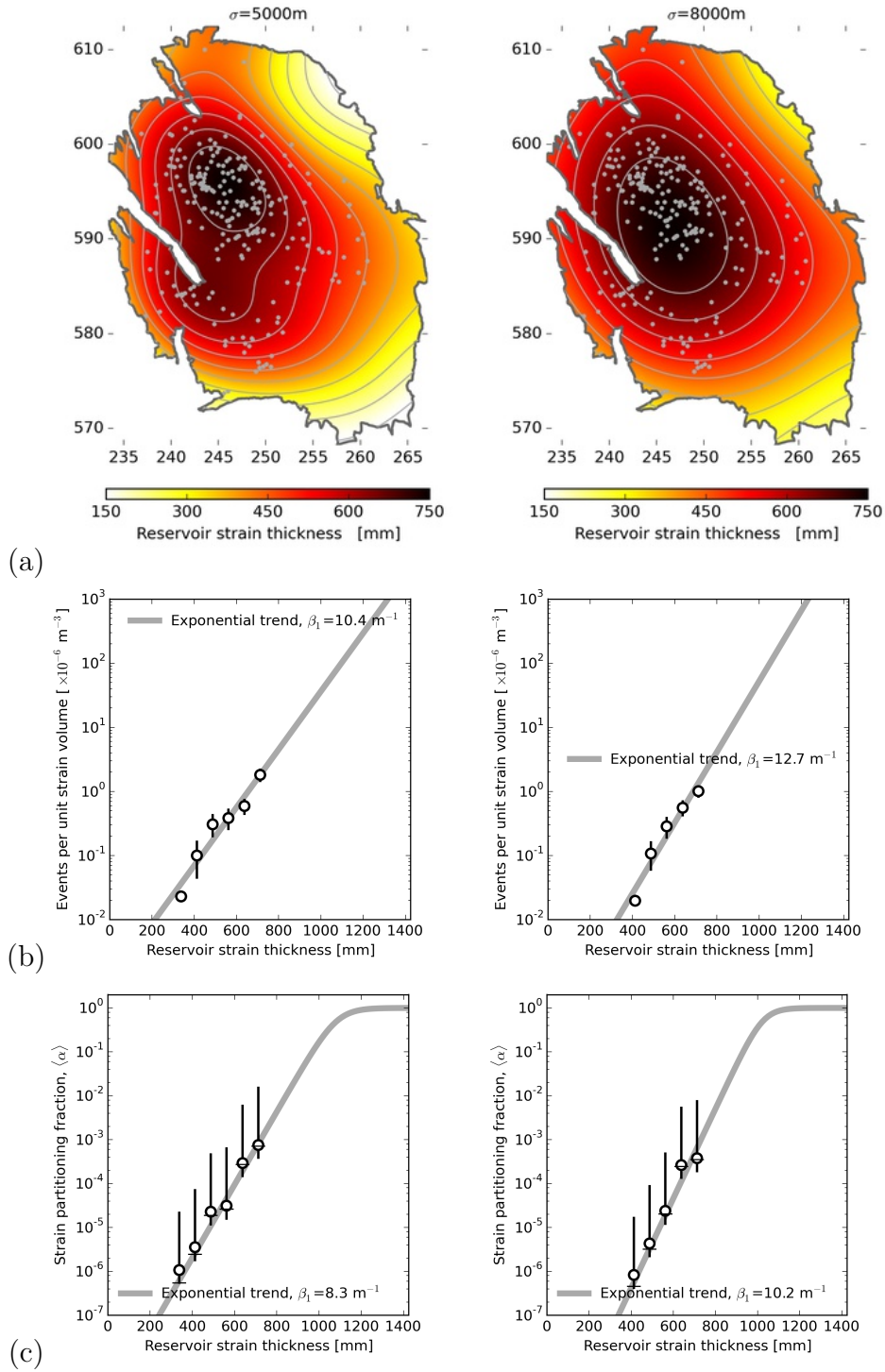


Figure 14: As Figure 12, except for $\sigma = 5000\text{ m}$ and 8000 m .

Figure 11 shows reservoir strain thickness maps for a range of increasing smoothness computed using a Gaussian filter kernel. This range starts with a smoothness length-scale, σ that is likely too small ($\sigma = 250\text{m}$) to be constrained by the observed earthquakes and ends with a smoothness length-scale that is likely too large ($\sigma = 5000\text{m}$) to explain the observed earthquakes. Variation in the apparent seismic activity rate and strain partitioning with reservoir strain thickness show exponential-like trends over a wide range of smoothing length-scales (Figures 12, 13, 14). These results are based on the reservoir strain thickness at the observed epicenter. A more complete assessment should include integrating over the entire strain thickness map weighted by the probability density function for the observed event location. This additional complexity in the assessment is currently ignored as

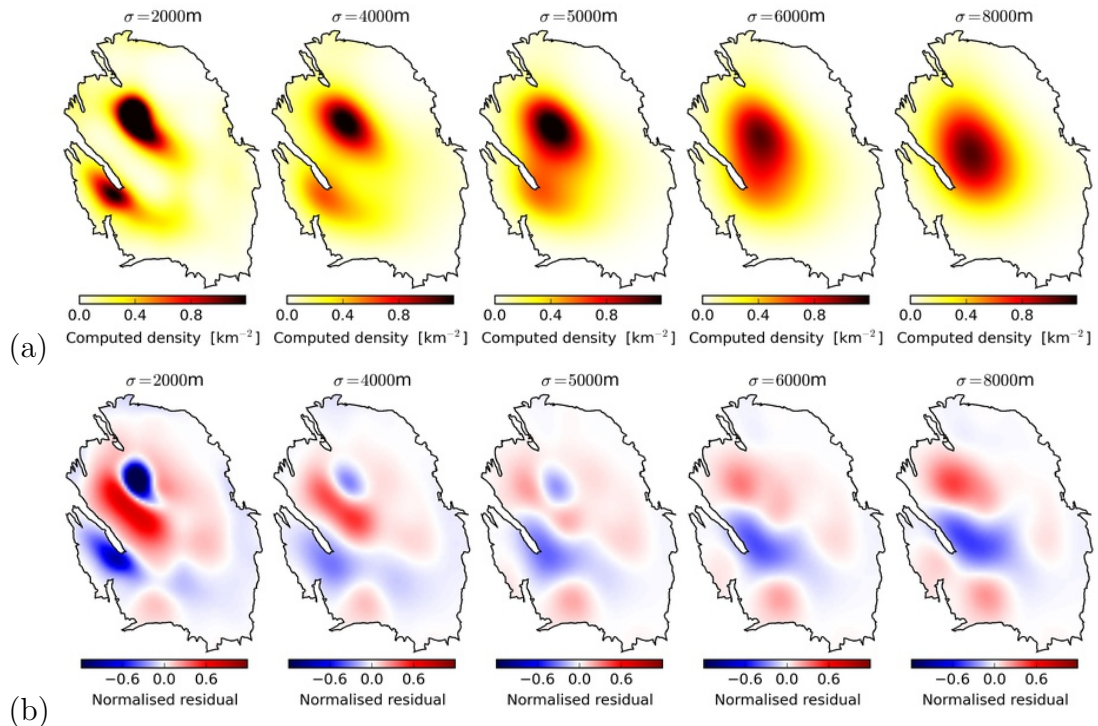


Figure 15: (a) Computed event density maps based on the thin-sheet strain-thickness model that has been smoothed using a Gaussian filter kernel with standard deviations (σ) from 2000 m to 8000 m. In each case, the maximum likelihood estimates for β_0 and β_1 were used to computed event density from the strain-thickness model. (b) Residuals between the observed and computed event densities. Positive residuals, shown in red, mean that the model over-predicted the local event density, and vice-versa for negative residuals, shown in blue.

this would reduce the resolution limit imposed by location errors but not the resolution limit imposed by the small sample size which will be subsequently shown to dominate.

For the smallest smoothing length-scale ($\sigma = 500$) the evidence for a coherent trend between activity rate and strain thickness, and between strain partitioning and strain thickness is weakest. This may be because the strain thickness model is wrong, or more likely because the epicenter location error is larger enough and the sample size small enough to obscure any underlying relationship. For larger smoothing length-scales the exponential-like trends in activity rate and strain partitioning become much more significant and robust across the remaining range of σ -values.

For each σ -value, we computed the maximum likelihood estimate for the activity rate model parameters (β_0, β_1). The slope of the exponential trend (β_1) governs the degree of localization of seismicity within the region of largest strain thickness, whereas the intercept (β_0) ensures the expected total number of events matches the observed total number. Based on these maximum likelihood estimates the activity rate model was used to compute the expected event density map for each σ -value and the corresponding residuals (Figure 12) with respect to the observed event density map (Figure 6). The $\sigma = 2000\text{m}$ results are clearly under-smoothed leading to over-localization of the computed event density as shown by a central region of over-prediction (blue residuals) surrounded by a ring of under-prediction (red residuals). In contrast, the $\sigma = 8000\text{m}$ results are clearly over-smoothed causing under-prediction (red residuals) of the largest observed event densities and over-prediction (blue residuals) across the band of little or no observed seismicity located just to the south and oriented northwest-southeast. Somewhere in between these extremes is an optimum σ -value that minimizes the residuals and maximizes the proportion of the observed variance explained by the model (PVE). Optimization of PVE based on a systematic grid search of σ -values between 2 and 8 km yields a global maximum of 0.9 corresponding to $\sigma = 5$ km (Figure 16a). A local maxima also exists at $\sigma = 4$ km (0.75) which is related to the bi-modal map distribution of computed event densities shown in Figure 15 that coalesce somewhere in the interval $4 \text{ km} < \sigma < 5 \text{ km}$.

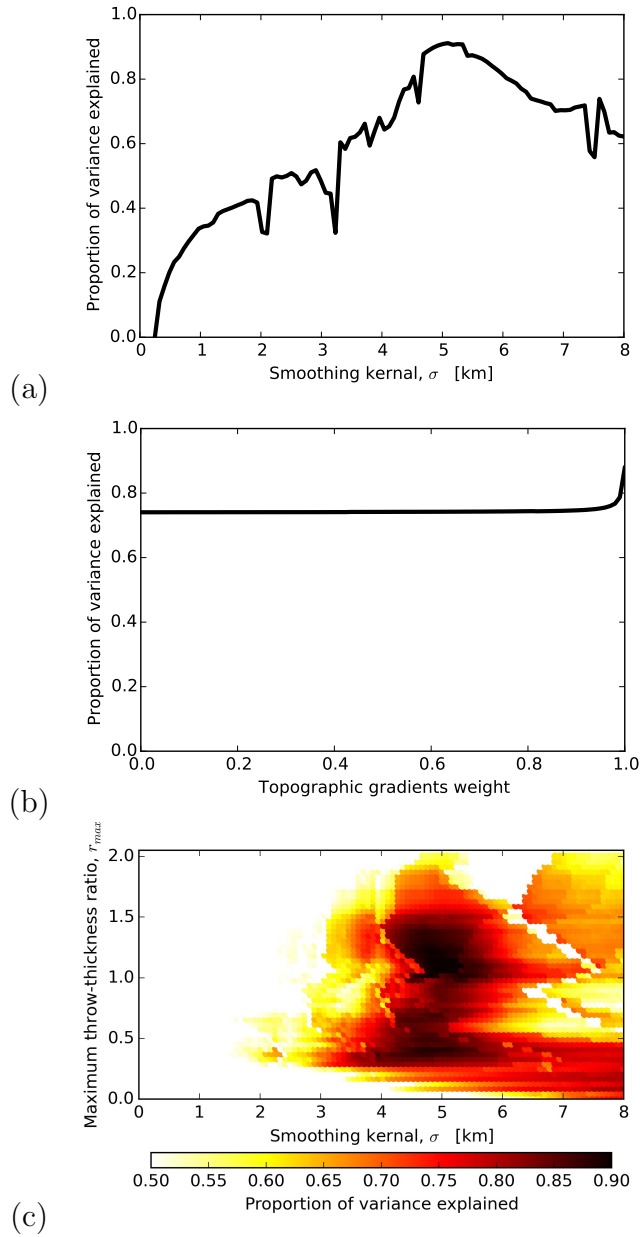


Figure 16: (a) Variation in performance of the thin-sheet strain-thickness model with the smoothing parameter, σ for unit topographic weight. Performance is measured as the fraction of observed variance explained by the model. This is maximal for $\sigma = 5$ km (0.9). (b) Variation in model performance with the topographic gradient weight for $\sigma = 5$ km and $r_{max} = 1$. (c) Variation in model performance with σ and the maximum fault throw to reservoir thickness ratio r_{max} indicates optimal values of $\sigma = 5$ km, $r_{max} = 1$.

3.7 Estimates of strain thickness model parameters

Three choices are required to uniquely define an instance of the thin-sheet strain thickness model. First, the σ -value that defines the smoothing length-scale. Second, the relative weight factor assigned to the topographic gradients (w_t) that defines the fraction of the total earthquake population originating on mapped faults. Third, the maximum fault throw to reservoir thickness ratio for faults (r_{max} included in the thin-sheet strain model. This allows for testing the possibility that only faults that do not completely offset the reservoir are seismogenic. A systematic grid search across all permutations of these parameters revealed little sensitivity to the choice of the topographic gradient weight with a slight preference for unit weight regardless of the other two choices (Figure 16b). There is some complexity in the trade-off between the other two choices (Figure 16c) due to the changing geometries of included faults and their influence on the smoothing outcomes. However, there is a clear optimal choice corresponding to $\sigma = 5$ km and $r_{max} = 1$. Excluding faults that do not completely offset the reservoir ($r_{max} < 1$ noticeably reduces the proportion of the variance explained. However, faults with slightly larger ratios ($1 < r < 1.5$) may be included in the model without significant performance degradation. Based on this evidence we proceed with a thin-sheet strain model for $\sigma = 5$ km, $w_t = 1$, and $r_{max} = 1$.

3.8 Estimates of activity rate model parameters

Maximum likelihood estimates, $\hat{\beta}_0$ and $\hat{\beta}_1$, and confidence regions based on relative likelihoods, for the parameter values of the exponential-trend Activity Rate (AR) model specified by (29) were obtained using the method described by Bourne and Oates (2014). These results (Figure 17) indicate a clear trade-off between the two parameters. This is attributed to the limited number of observed events and the limited range of observed variation in reservoir strain thickness. Uncertainty in the exponential exponent, β_1 , will particularly influence how this model extrapolates to the larger values of reservoir strain thickness anticipated in the near future. The largest and smallest values of $\hat{\beta}_1$ represent upper and lower bounds respectively for this epistemic uncertainty. With time, this uncertainty is expected to reduce as the number of observed events and the range of observed reservoir strain thickness increases. Monte Carlo simulations of future seismicity take account of these current uncertainties by sampling the distribution of parameter estimates according to their relative likelihoods.

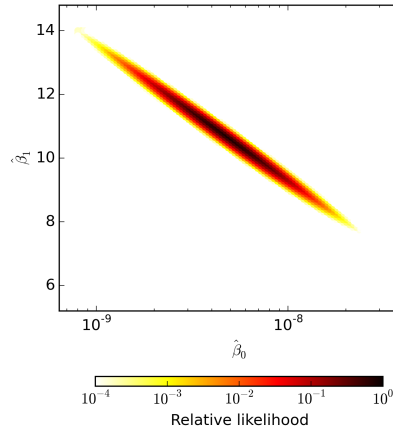


Figure 17: Maximum likelihood estimates for the exponential-trend model parameters yield $\hat{\beta}_0 = 5.3 \times 10^{-9} \text{ m}^{-1}$ and $\hat{\beta}_1 = 10.2 \text{ m}^{-1}$. Relative likelihoods indicate confidence regions surrounding this estimate.

3.9 Estimates of aftershock model parameters

Earthquake populations typically include aftershocks and the same is true for the Groningen earthquakes (Bourne and Oates, 2014). These aftershocks are modeled using the Epidemic Type Aftershock Sequence (ETAS) model (Ogata, 1998, 2011) that comprises a temporal trigger function, a spatial triggering function, and a magnitude triggering function. The temporal and spatial triggering functions are represented as inverse power-laws defined by characteristic values (c , d) and exponents (p , q). The magnitude triggering function is represented as exponential function defined by a scaler (K) and an exponent (a). Joint maximum likelihood estimates for the ETAS and AR parameter values and their confidence regions were obtained using the method described by Bourne and Oates (2014). The distributions of acceptable solutions given the observed events and the selected reservoir strain thickness model are summarized in Figure 18.

In the limit that $K = 0$, the ETAS model generates no aftershocks. The maximum likelihood estimate is $\hat{K} = 0.1$ and the relative likelihood of $K = 0$ is less than 10^{-4} . This indicates there is significant evidence for aftershocks in the Groningen earthquake catalogue and simulations of future seismicity should therefore include these aftershocks. Probabilistic simulations of future seismicity based on this AR-ETAS model are computed by sampling these parameter estimate distributions according to their relative likelihoods.

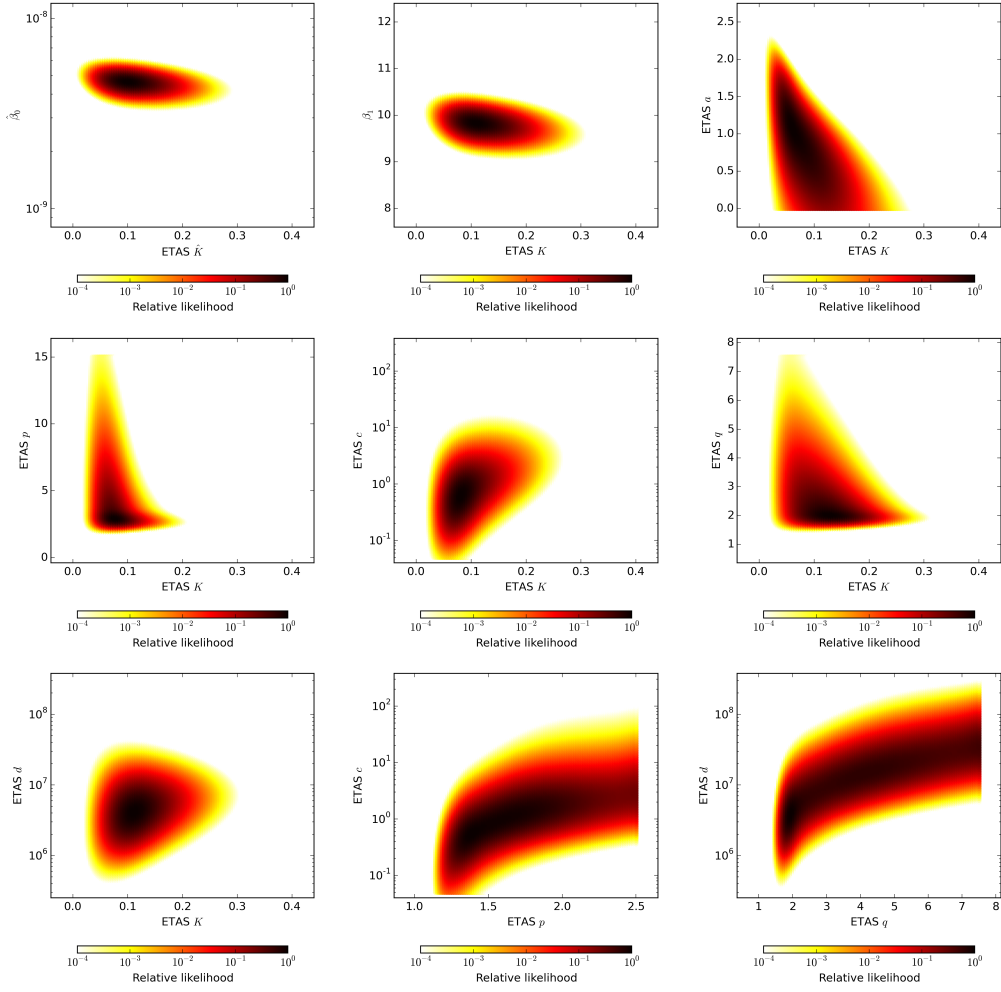
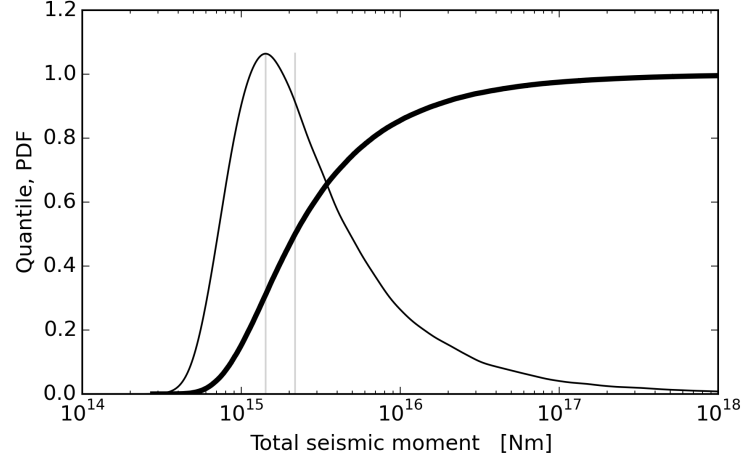
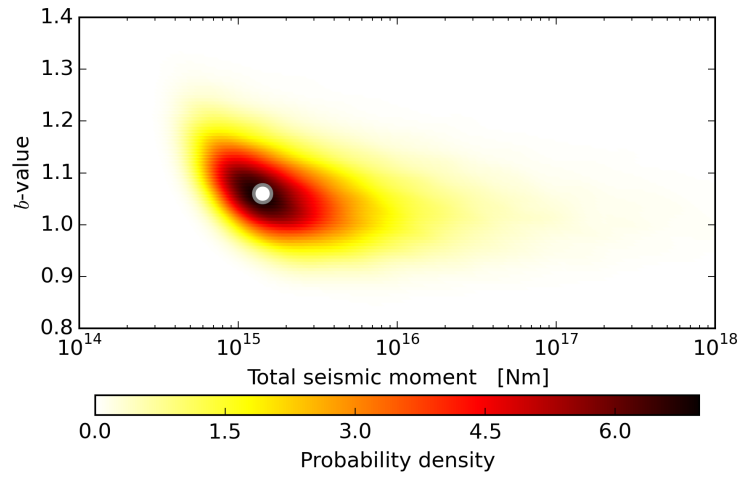


Figure 18: A selection of slices through the relative likelihood distribution around the maximum likelihood parameter estimates. White dots denote the maximum likelihood parameter estimates for $\beta_0, \beta_1, K, p, q, d$ subject to the constraint $c = 3$ days and $d = 5 \times 10^6$ m².



(a)



(b)

Figure 19: (a) Probability distribution of the total seismic moment of $N = 239$, $M_L \geq 1.5$ independent magnitudes sampled from a frequency-magnitude distribution with $b = 1.06$ based on 10^5 simulated catalogues. The modal value exactly matches the observed total seismic moment of 1.4×10^{15} Nm for the 239 $M_L \geq 1.5$ events observed from 1 April 1995 to 18 January 2015. For reference, the second vertical grey line located to the right of the modal value denote the median of this distribution which is 1.5 times larger than the modal value. (b) The joint probability distribution of total seismic moment and b -value for $N = 239$ events. The white circle denotes the total seismic moment and b -value estimated from the observed $N = 239$, $M_L \geq 1.5$ events.

3.10 Estimates of b -value

The maximum likelihood estimate of the b -value that describes the slope of the frequency-magnitude distribution for all 239 $M_L \geq 1.5$ observed between 1 April 1995 and 18 January 2015 is $\hat{b} = 0.96$ with a 95% confidence interval of $0.8 < \hat{b} < 1.1$.

Stochastic simulation of $N = 239$ events independently sampled from the frequency-magnitude distribution with constant b -value produces a single realization of the catalogue of event magnitudes. Repeating this simulation 10^5 times yields a stable estimate for the probability distribution of the total seismic moment and apparent b -value for these simulated catalogues. The total seismic moment is a Pareto sum distribution with a heavy right-side tail (Figure 19a). This means the median value is about 1.5 times larger than the modal value and confidence interval about the modal value are significantly skewed extended further above than below the modal value. The constant b -value selected for these simulations is $b = 1.06$, which is slightly larger than the maximum likelihood estimate for reasons that will be discussed shortly.

The apparent b -value for each simulated catalogue does not exactly equal the asymptotic limit of the parent distribution ($b = 1.06$) due to the finite sample size ($N = 239$), but instead is distributed about this value in a manner that is negatively correlated with the total seismic moment (Figure 19b) and

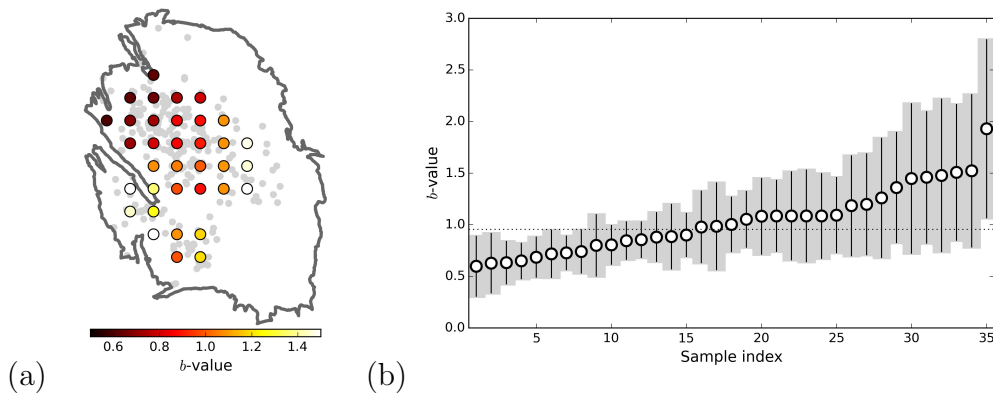


Figure 20: (a) Maximum likelihood estimates of b -value for $M_L > 1.5$ events between 1 April 1995 and 18 January 2015 within 9×9 km overlapping box-shaped regions spaced every 3 km and containing at least 15 events. Grey circles denote the epicenters of these events. (b) 95% confidence intervals for these same b -value estimates arranged in ascending order. A dashed line denotes the maximum likelihood b -value estimated from the entire population which is consistent with the b -values estimated for most spatial subsets except for the few most extreme values.

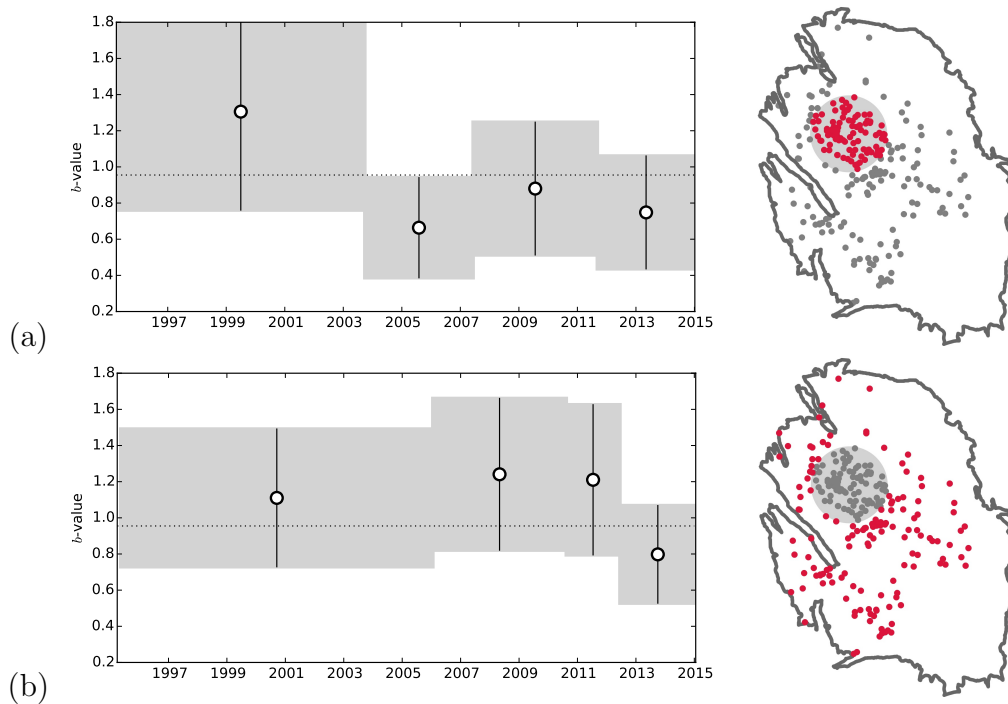


Figure 21: Maximum likelihood estimates of b -value through time for $M_L \geq 1.5$ events between 1 April 1995 and 18 January 2015. (a) Events within 5 km of the center of seismicity (93 events), (b) Events beyond 5 km from the center of seismicity (146 events). The center of seismicity is taken to be located at 245 km east and 596 km north. Vertical error bars denote the standard 95% confidence interval, grey regions denote the temporal and spatial bins. The dotted line shows the b -value estimated for the whole population ($b = 0.96$).

varies from below 0.9 to above 1.2. This stochastic variation in the simulated b -values is similar to the 0.8 to 1.1 confidence interval on the b -value estimated from the observed magnitudes.

For the modal (maximum likelihood) value of this distribution to match the observed total seismic moment we note that this requires $b = 1.06$. This is slightly above the maximum likelihood estimate for the b -value but within its 95% confidence interval. One reason for this is that the observed magnitudes may not conform to the assumption underlying the maximum likelihood estimate of independent and identically distributed magnitudes. Previous analysis showed no current evidence for correlations between the observed magnitudes, although the event locations and origin times do show correlations. This apparent behavior of clustered epicenters and origin times but independent magnitudes is also typical of natural earthquake populations (Felzer and Abercrombie, 2004).

The remaining assumption of identically distributed magnitudes may be assessed by testing for statistically significant differences in b -value for different subsets of the data. The strength of these tests will of course be limited because of small total number of observed events. Nonetheless, these tests are important as any emerging evidence for systematic changes in b -value with location, or time, or reservoir deformation, or some other metrics may be influential on the assessed seismic hazard or risk.

Estimates of b -values within different spatial subsets (Figure 20) indicate an apparent spatial trend with the smallest values mostly located in regions with the larger event densities and therefore smaller confidence bounds. Compared to the b -value for the entire population most of this apparent spatial trend in b -values is not significant at the 95% confidence level, with the possible exception of the most extreme b -values.

The possible time-dependence of b -values was assessed in a similar fashion, by computing the maximum likelihood estimate for events within disjoint time blocks for two distinct spatial domains centered on the area of greatest seismicity (Figure 21). On this occasion to avoid any possible bias due to different sample size, each time blocks were selected to ensure an equal number of events in each block. These results suggest an apparent trend of decreasing b -values with time. However, there are a few counter-examples of apparent b -value increasing with time. Moreover, with just one exception, all these estimates are consistent with a constant b -value estimated from the whole population ($b = 0.96$) within their 95% confidence intervals.

To look for any trend in b -values with reservoir deformation which varies in both space and time, each event was labeled with the value of reservoir strain thickness at the location of its epicenter at the end of the time period under consideration (18 January 2015). These events were then sequenced

according to strain thickness and then divided into disjoint bins with, as far as possible, equal populations. Figure 22 shows the results where the arbitrary choice of the number of bins was varied systematically from 1 to 12. The smaller numbers of bins provide too little sampling of any variation with reservoir strain thickness and the larger numbers of bins provide too little confidence in the estimated b -values due to the small number of events within each bin. Somewhere in between there is a balance between these two limiting effects that suggests a trend of b -value decreasing with reservoir strain thickness. This trend is apparent in all cases with at least 2 bins, however we do note that the 95% confidence bounds associated with these estimates are for the most-part also consistent with a constant b -value.

Overall, the current evidence for any changes of b -values with location, time, or reservoir deformation is not compelling but equally the evidence does not support rejecting this possibility. Indeed, there is some existing evidence for b -values decreasing with increasing differential stress; for instance prior to the occurrence of larger earthquakes (Tsukakoshi and Shimazaki, 2008; Nanjo et al., 2012), and also with increasing depth (Mori and Abercrombie, 1997; Spada et al., 2013). To account for both possibilities two scenarios for the future development of the b -value will be considered. The first scenario is a constant b -value consistent with the maximum likelihood estimate but then revised upwards slightly to match the observed cumulative total seismic moment. The second scenario is a b -value that decreases with reservoir strain thickness according to the hyperbolic function shown in Figure 22. A hyperbolic function was selected to represent a monotonic transition between two bounding values such that

$$b(c_t) = \left(\frac{b_1 + b_2}{2} \right) - \left(\frac{b_1 - b_2}{2} \right) \tanh \left(\frac{c_t - c_0}{c_1} \right), \quad (31)$$

where b_1 , b_2 are the initial and final bounds of the b -value, c_0 is the value of reservoir strain thickness at the mid-point of the transition, and c_1 is a parameter governing the length-scale of this transition.

Model parameters were estimated given the observed joint distribution of N event magnitudes and reservoir strain-thickness values corresponding to the epicenter and origin time of each event using Bayesian inference. The log-likelihood function for this model is simply an extension of the log-likelihood function, ℓ , for a constant b -value (*e.g.* Aki, 1965; Utsu, 1966; Gibowicz and Kijko, 1994),

$$\ell(b_1, b_2, c_0, c_1) = \sum_{i=1}^N \ln b(c_{t,i}) - \sum_{i=1}^N b(c_{t,i})(M_i - M_{min} + \Delta M/2), \quad (32)$$

where M_i is the magnitude of the i^{th} event, M_{\min} is the minimum magnitude of events considered in the analysis which corresponds to the magnitude of completeness, and ΔM is the bin size used for reporting magnitudes. In our case $M_{\min} = 1.5$ and $\Delta M = 0.1$. The b -value, $b(c_{t,i})$ now depends on reservoir strain thickness according to 31.

Independent uniform prior distributions were assigned to each model parameter b_1, b_2, c_0, c_1 . For b_1 and b_2 these ranged between 0.5 and 1.5 to cover the range of generally acceptable values. The range for c_0 and c_1 were set to $[0, 0.6]$ and $[0.01, 0.2]$ respectively. These were selected to be positive definite and to cover a broad enough range such that the results were not sensitive to the choice.

The resulting posterior distributions (Figure 23) indicate a wide spread of possible b -value trends including a constant b -value, or a b -value that increases or decreases with increasing reservoir strain. This is unsurprising given the small number of events available for analysis limit the precision

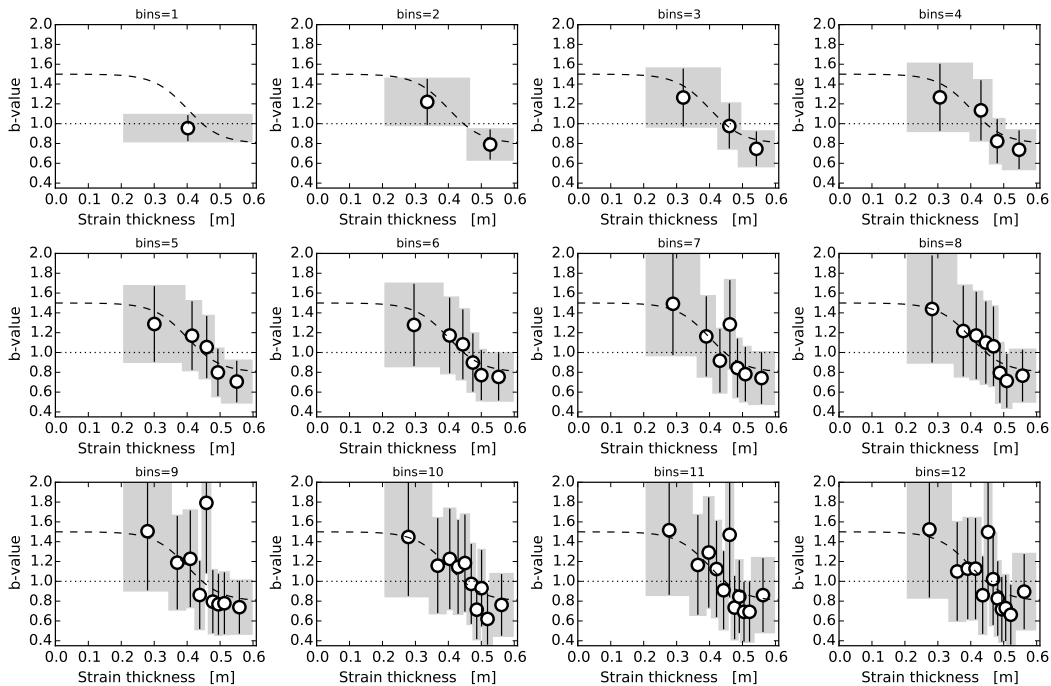


Figure 22: Estimation of b -value as a function of reservoir strain thickness. Vertical error bars denote the standard 95% confidence interval, grey regions denote the temporal bins. The dashed line denotes an example hyperbolic tangent function as a possible model for changes in b -value with strain thickness.

of b -value estimates as previously shown in Figure 22. The maximum a posterior probability density corresponds to a maximum decrease in b -value of 0.7 (Figure 23c) from 1.35 to 0.65 (Figure 23d). However, the median b -value from the marginal distribution for a given strain thickness shows only a small decrease from 1.0 to 0.95 (Figure 23a), whereas the 95% confidence interval shows a more pronounced decreasing trend such that b -values as small as 0.6 are much more likely for the largest values of reservoir strain thickness. Despite these possibilities of systematic variations in b -value with reservoir strain thickness, the overall distribution of b -values (Figure 23a) is similar to that obtained for a constant b -value (Figure 19).

For these reasons, the influence of systematic changes in b -value with strain on short-term seismicity forecasts maybe modest. This might be because the true physical process does not cause any such variation or because the current level of uncertainty due to the small sample size of historic events mostly masks the true systematic trend in b -value. In order to assess the sensitivity to this model choice, both the constant b -value and the decreasing b -value models were used for independently simulating historic and future seismicity.

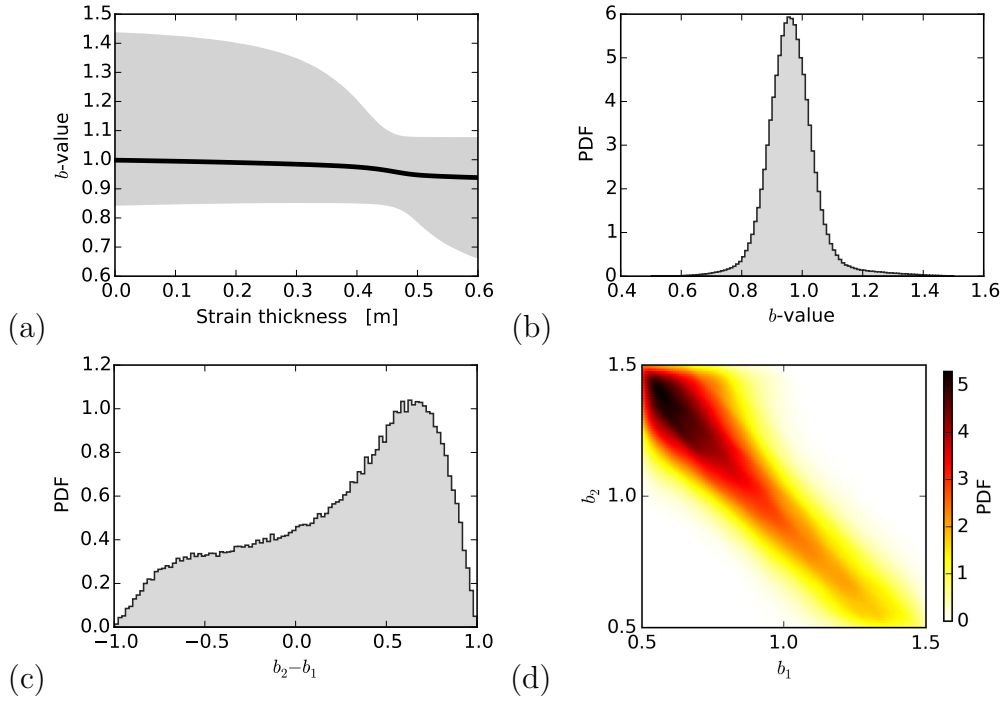


Figure 23: Posterior distributions of parameter values for the strain-dependent b -value model according to (31) given the observed magnitudes and the reservoir strain thickness at the origin time and epicenter of the events. (a) The median b -value trend with reservoir strain thickness (black line) and the 95% confidence region (grey region). (b) Posterior distribution of b -values for all values of strain thickness. (c) Posterior distribution for the maximum change in b -value ($b_2 - b_1$) with increasing strain thickness. (d) Joint posterior distribution for b_1 and b_2 .

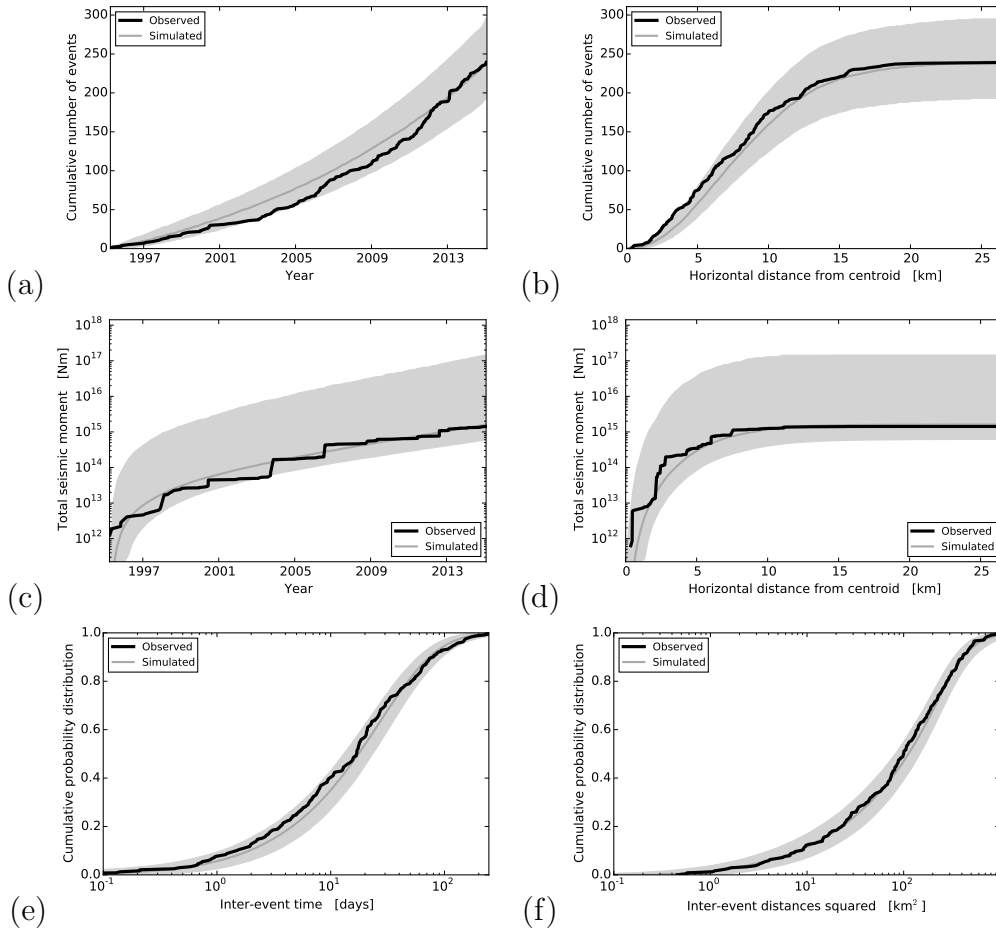


Figure 24: Simulation results from the exponential compaction trend Poisson process model with aftershocks and the strain-dependent b -value model. (a) The cumulative number of $M \geq 1.5$ events observed through time between April 1995 and August 2014 as a function of time. (b) As (a) except for the horizontal distance from the centroid of the observed locations. (c, d) As (a, b) except for total seismic moment. (e, f) The inter-event times and distances-squared provide a measure of temporal and spatial clustering respectively. The simulated results are shown as the median and the 95% confidence interval. These results were obtained from 10^4 catalogues simulated according to the exponential compaction trend Poisson model and a standard random location error of 500 m. Model parameter estimates were sampled from the relative likelihood distribution shown in Figure 17. In this case the simulations are based on independent samples from a frequency-magnitude distribution with a b -value as a function of strain thickness, $M_{min} = 1.5$, $M_{max} = 6.5$ initially, and a standard magnitude error of 0.2.

3.11 Stochastic simulation of historic seismicity

Stochastic simulations of earthquake catalogues over the period of observed seismicity provides a useful opportunity to measure the performance of the seismological model, to quantify uncertainties, and to identify any further opportunities for improving the model. Figure 24 shows the results of such simulations in terms of the cumulative distribution of event numbers and magnitudes in time and space as well as their temporal and spatial clustering due to aftershocks. In each case the observed seismicity is similar to the median simulation and within the 95% confidence interval of all the simulations.

The influence of switching from the strain-dependent b -value model to the constant b -value model is really quite minor (Figure 25); the key difference is limited to the upper bound of the total seismic moment increasing at a slightly greater rate with time for the strain-dependent b -values. This limited difference is not surprising given the current weakness in the evidence for any systematic decrease in b -values (Figure 22).

Likewise the observed annual event count and total seismic moments are consistent with the simulation results (Figure 26). The observed secular trend of increasing seismicity is matched by the median simulation and the observed year-to-year variability is matched by the 95% confidence interval of all the simulations. This 95% confidence interval applies independently to each individual year, so the number of exceedances over the 20 years of observation will be binomially distributed. This means there is just a 0.36 chance of no years exceeding the 95% confidence interval, and likewise a 0.64 chance of at least one exceedance and a 0.26 chance of at least two exceedances. Compared to this, the simulated 95% confidence intervals seem credible as the annual event numbers and total seismic moments show two and zero exceedances respectively.

Figure 27 compares the observed and simulated event density maps in 2015 whilst Figure 29 compares the observed epicenters with the model-based expected event density for each year of observation. The median simulation density does exhibit some residuals relative to the observed event density map (Figure 27). This is mostly characterized by under-prediction (red residuals) within a northwest-southeast extended region in the vicinity of the greatest observed event density. This is balanced by over-prediction (blue residuals) in the nearby flanks to the northeast and particularly to the southwest. However, the observed event density distribution is almost entirely inside the 95% confidence interval of the simulated seismicity indicating these residuals are likely insignificant. This is a significant improvement compared to the earlier activity rate model based on reservoir compaction (Bourne and Oates,

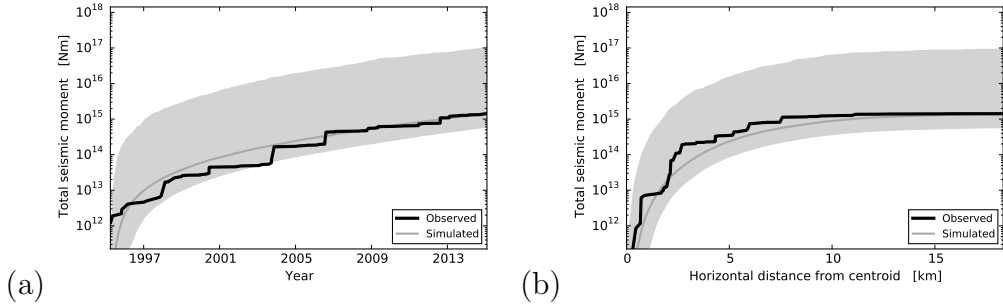


Figure 25: As for Figure 24, except for the constant b -value model. As this model is identical to the strain-dependent b -value model in all respects except for event magnitudes, only the distributions of total seismic moment are shown.

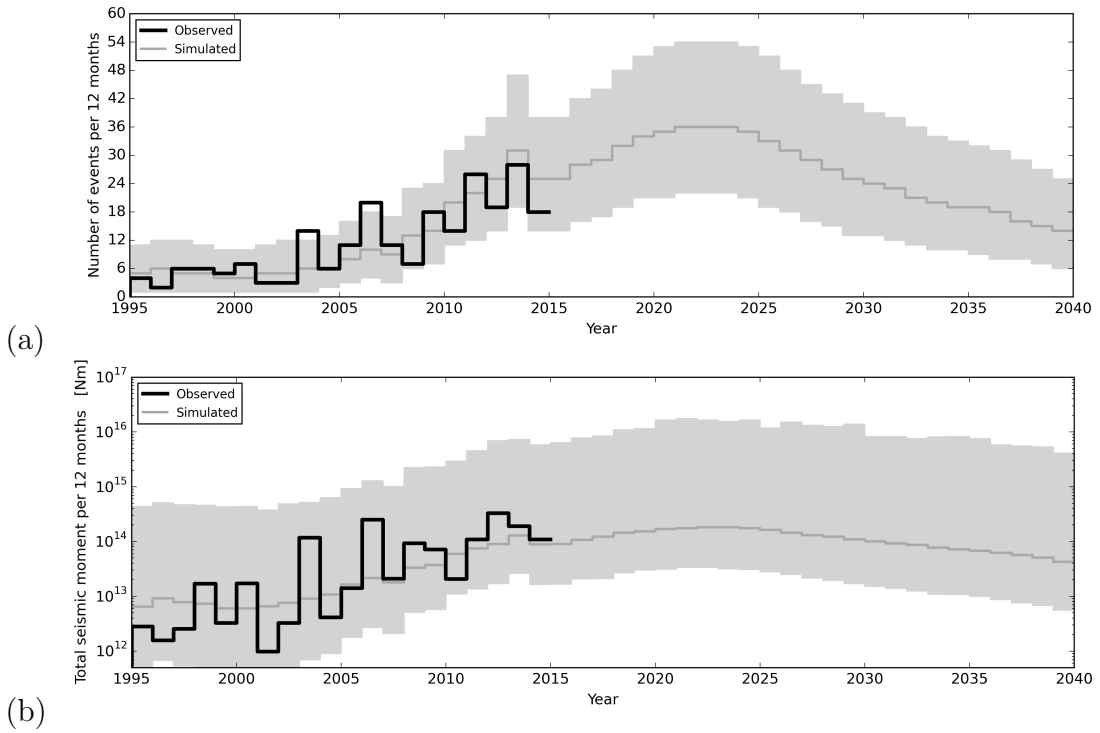


Figure 26: History match and forecast based on 10,000 simulations from the extended activity rate model with aftershocks and a strain-dependent b -value given the linear compaction model excluding its uncertainty. (a) Observed annual event rate compared to simulations. (b) Observed annual total seismic moment compared to the same simulations. Grey regions denote the 95% confidence interval of the simulations.

2014). Nonetheless, the spatial coherence of these residuals does indicate an opportunity to improve the seismological model, perhaps by updating the compaction model using all the available levelling, InSAR, and GPS data or by extending the simple geometric criteria used to identify which faults are seismogenic. Once the upgraded earthquake monitoring network is operational the expected improvement to detection sensitivity ($M \geq 0.5$) and epicenter location accuracy ($\pm 50\text{m}$) will significantly improve our ability to identify which faults are most seismogenic within the induced strain field.

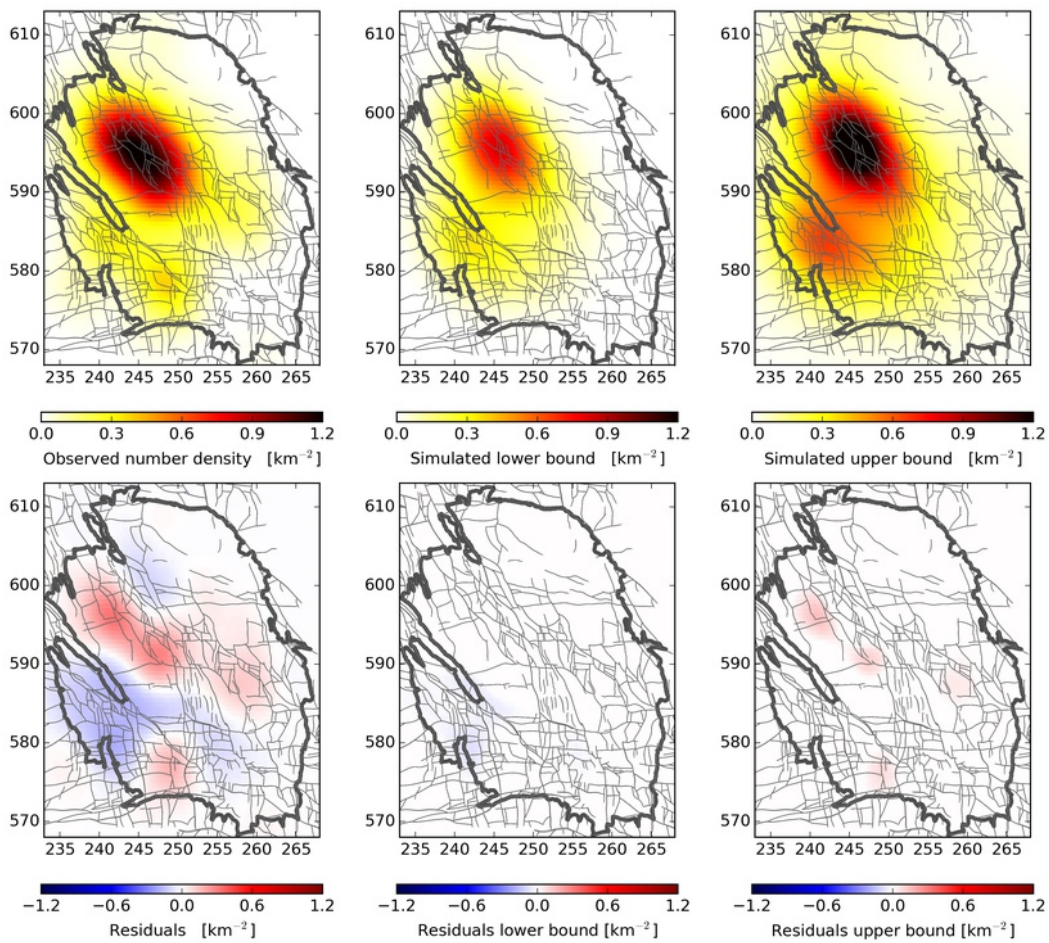


Figure 27: Maps of the observed and simulated number density and the residuals between them. Events densities were computed using the Gaussian kernel method. Simulation results were obtained using the full probability distribution of parameter estimates for the exponential compaction trend activity rates with epidemic type aftershock sequences.

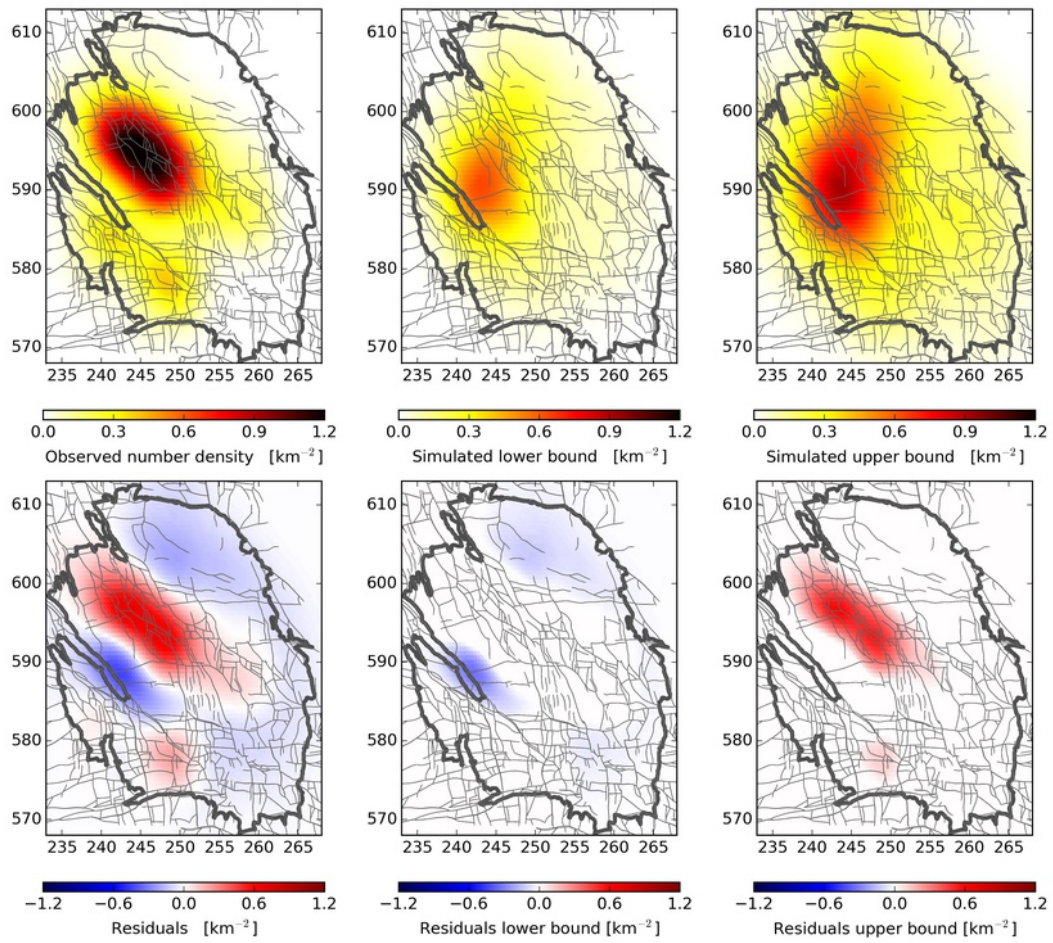


Figure 28: As Figure 27, except for the previous Activity Rate model based on reservoir compaction (Bourne and Oates, 2014).

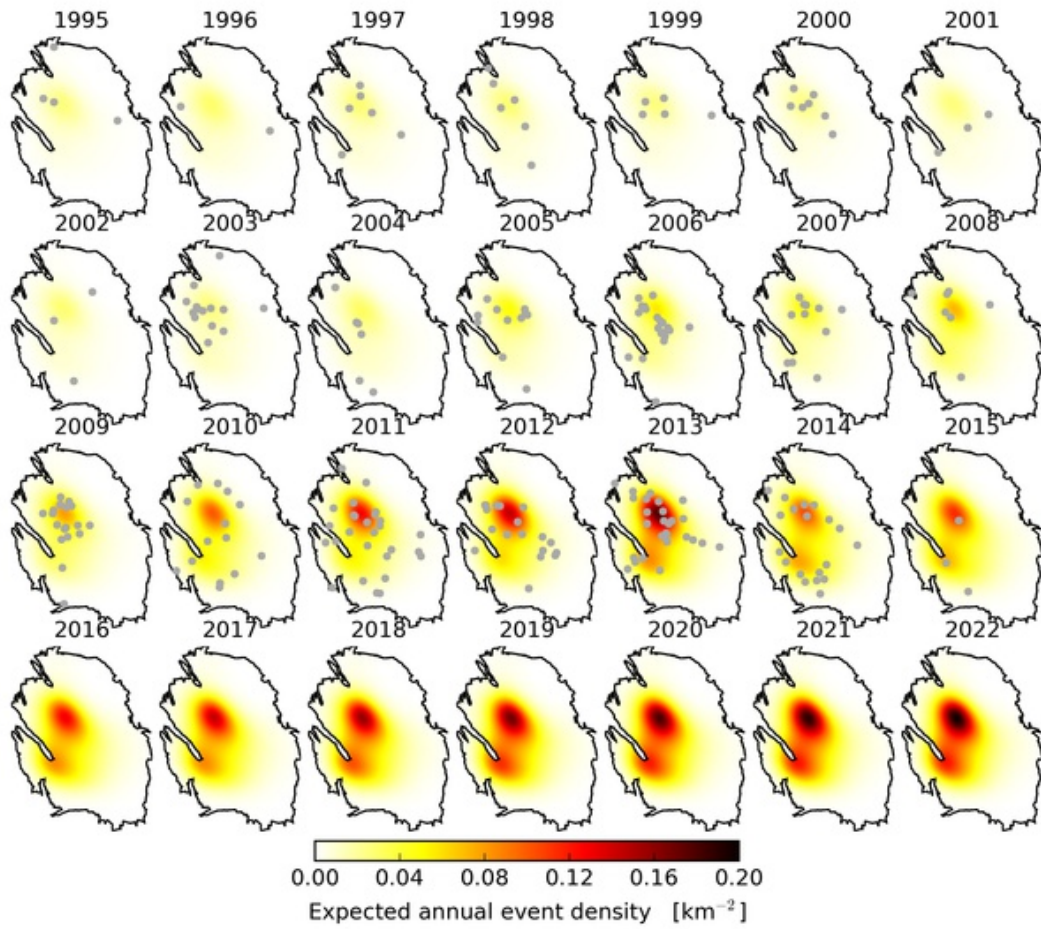


Figure 29: Observed annual epicenters compared to the activity rate model expected annual event density maps.

4 Discussion & Conclusions

To a first approximation the seismicity within the Groningen field is organized according to the uni-axial scalar strain field (reservoir compaction) as the induced earthquake population plays its part in accommodating the induced reservoir strains (Bourne et al., 2014; Bourne and Oates, 2014). Extending this model to the uni-axial tensor strain field allows for the inclusion of additional strain mechanisms due to lateral gradients in reservoir thickness, reservoir compaction, and top reservoir topography. In the case of the Groningen gas reservoir, these first two mechanisms are negligible, and the last mechanism is primarily controlled by pre-existing faults that partially offset the reservoir. This thin-sheet strain model of the reservoir provides a framework for extending the activity rate model of seismicity induced by reservoir compaction (Bourne and Oates, 2014) to include a role for faults.

Pre-existing faults that offset the reservoir cause a geometric localization of strain induced by reservoir compaction. Accumulation of strain around these faults is thought to increase the likelihood of fault slip, although not all fault slip may be seismogenic, for instance if the fault creeps instead. Pre-existing faults subject to the largest reservoir compaction and with offsets that do not exceed the local reservoir thickness were found to be mostly likely associated with historic seismicity. Fault with larger offsets appear to be either stable or slipping aseismically. This difference in fault behaviour might be due to the juxtaposition of different geological formations on either side of the fault, such as the Rotliegendes sandstone juxtaposed to the Zechstein salt formation. Another possibility is the smearing or intrusion of ductile materials, such as clay or anhydrite, along the fault surface during previous fault slip events, with the quantity, spatial extent and mechanical influence of this material on the fault increasing with fault offset.

The limited number of observed events and the standard epicentral location error (*c.* 500 m) places a fundamental limit on the observable resolution of the seismological model. This means, given the currently available information, the seismological model is only capable of spatially smooth forecasts of future seismicity. Optimization of this smoothing parameter indicates a value of 5 km. This is not necessarily such a fundamental limit on the spatial resolution of the probabilistic seismic hazard and risk analysis as earthquake ground motion accelerations are likely correlated on a length-scale comparable to the depth of the reservoir (3 km).

In summary, the extended activity rate model yields simulations of the historic seismicity that match the observed spatial-temporal distribution of event occurrences and magnitudes and inter-event clustering within their stochastic variability without any significant bias. If this past relationship

between reservoir compaction, reservoir fault geometries and induced seismicity continues then the extended activity rate model offers a reliable basis for probabilistic earthquake forecasting at least in the short term. As gas production and induced seismicity continues and more data becomes available through monitoring the validity of this model should be reassessed and, if necessary, revised to ensure it continues to offer a reliable basis for short-term seismicity forecasting.

5 Recommendations for further work

We identify the following opportunities for further improvements to the seismological model:

- Reassess the role of faults within the field of reservoir compaction following updates to the compaction model based on the joint inversion of all available levelling, InSAR and GPS measurements of surface displacement.
- Investigate the utility of allowing the weight parameter w_t to become a function of geographical position, such as correlated with some measure of fault density.
- Incorporate uncertainty in the forecast values of reservoir compaction into the seismological model.
- Investigate statistical mechanics models of failure avalanches such as fiber bundle models (*e.g.* Pradhan, 2010) as a physical basis for the exponential-like increase in activity rates with reservoir compaction, the power-law distribution of earthquakes, the presence of aftershocks sequences, and the systematic decreases in b -values with increasing deformation.
- Investigate the evidence for possible time-delay or non-linear strain rate effects on the nucleation rate or the b -value of induced seismicity.
- Extend the seismological model to forecast focal mechanisms and finite ruptures to test the sensitivity of probabilistic seismic risk assessment to finite ruptures. Consider how ruptures may extend into the basement and the potential influence of triggered seismicity.

Acknowledgements

We are grateful to Julian Bommer, Rick Wentinck, Peter van den Bogart for useful discussions about seismicity and to Stijn Biermann and Famke Kraaijeveld for sharing their insight on reservoir compaction. We appreciate the detailed and careful review of this report by Chris Harris; his constructive suggestions allowed us to make several improvements. The implementation of this extended Activity Rate model made use of SciPy (Jones et al., 2001) and most of the figures were created using Matplotlib (Hunter, 2007).

References

- Aki, K., 1965. Maximum likelihood estimation of b in the formula $\log N = a - bM$ and its confidence limits. *Bulletin of the Earthquake Research Institute of Tokyo University* 43, 237–239.
- Bierman, S., Kraaijeveld, F., Bourne, S., 2015. Regularised direct inversion to compaction in the Groningen reservoir using measurements from optical leveling campaigns. Technical Report. Shell Global Solutions International. Amsterdam.
- Bourne, S.J., Oates, S.J., 2014. An activity rate model of induced seismicity within the Groningen field (draft). Technical Report. Nederlandse Aardolie Maatschappij. Assen, The Netherlands.
- Bourne, S.J., Oates, S.J., Bommer, J.J., Dost, B., Elk, J.V., Doornhof, D., 2015. A Monte Carlo Method for Probabilistic Hazard Assessment of Induced Seismicity due to Conventional Natural Gas Production. *Bull. Seis. Soc. Am.* 105.
- Bourne, S.J., Oates, S.J., van Elk, J., Doornhof, D., 2014. A seismological model for earthquakes induced by fluid extraction from a subsurface reservoir. *J. Geophys. Res. Solid Earth* 119.
- Felzer, K.R., Abercrombie, R.E., 2004. A Common Origin for Aftershocks, Foreshocks, and Multiplets. *Bull. Seis. Soc. Am.* 94, 88–98.
- Gibowicz, S., Kijko, A., 1994. *An Introduction to Mining Seismology*. Academic Press.
- Hunter, J.D., 2007. Matplotlib: A 2D graphics environment. *Computing In Science & Engineering* 9, 90–95.
- Jones, E., Oliphant, T., Peterson, P., 2001. SciPy: Open source scientific tools for Python. <http://www.scipy.org/>.
- Kostrov, V.V., 1974. Seismic moment and energy of earthquakes, and seismic flow of rocks. *Izv. Acad. Sci. USSR Phys. Solid Earth*, 1, Eng. Transl., 23–44.
- Mori, J., Abercrombie, R., 1997. Depth dependence of earthquake frequency-magnitude distributions in California: Implications for rupture initiation. *Journal of Geophysical Research* 102, 15,081–15,090.

- Nanjo, K.Z., Hirata, N., Obara, K., Kasahara, K., 2012. Decade-scale decrease in b value prior to the M 9-class 2011 Tohoku and 2004 Sumatra quakes. *Geophysical Research Letters* 39, n/a–n/a.
- Ogata, Y., 1998. Space-time point-process models for earthquake occurrences. *Ann. Inst. Statist. Math.* 50, 379–402.
- Ogata, Y., 2011. Significant improvements of the space-time ETAS model for forecasting of accurate baseline seismicity. *Earth, Planets and Space* 63, 217–229.
- Pradhan, S., 2010. Failure Processes in Elastic Fiber Bundles. *Rev. Mod. Phys.* 82, 449–. [arXiv:0808.1375v3](https://arxiv.org/abs/0808.1375v3).
- Spada, M., Tormann, T., Wiemer, S., Enescu, B., 2013. Generic dependence of the frequency-size distribution of earthquakes on depth and its relation to the strength profile of the crust. *Geophysical Research Letters* 40, 709–714.
- Tsukakoshi, Y., Shimazaki, K., 2008. Decreased b-value prior to the M 6 . 2 Northern Miyagi , Japan , earthquake of 26 July 2003. *Earth Planets Space* 60, 915–924.
- Utsu, T., 1966. A statistical significance test of the difference in b-value between two earthquake groups. *Journal of Physics of The Earth* 14, 37–40.